Applied Materials Today 31 (2023) 101750

Contents lists available at ScienceDirect

Applied Materials Today

journal homepage: www.elsevier.com/locate/apmt

Gold-iron oxide nanoparticle: A unique multimodal theranostic approach for thrombosis

Najma Annuria Fithri [a,b,c], Yuao Wu [a], Gary Cowin [d], Fahima Akhter [a], Huong D.N. Tran [a], Brian Tse [e], Nicholas Westra van Holthe [d], Shehzahdi S. Moonshi [a], Karlheinz Peter [f,g,h,i], Xiaowei Wang [g,h,i,j], Nghia P. Truong [b,*], Hang Thu Ta [a,k,l,*]

[a] Queensland Micro and Nanotechnology Centre, Griffith University, Brisbane, Australia
[b] Faculty of Pharmacy and Pharmaceutical Sciences, Monash University, Melbourne, Australia
[c] Department of Pharmacy, Sriwijaya University, Indralaya, Indonesia
[d] Centre for Advanced Imaging, the University of Queensland, Brisbane, Australia
[e] Translational Research Institute, Brisbane, Australia
[f] Atherothrombosis and Vascular Biology Laboratory, Baker Heart and Diabetes Institute, Melbourne, Australia
[g] Department of Cardiometabolic Health, The University of Melbourne, Parkville, Victoria, Australia
[h] Department of Medicine, Monash University, Melbourne VIC, Australia
[i] Baker Department Cardiovascular Research, Translation and Implementation, La Trobe University, Melbourne VIC, Australia
[j] Molecular Imaging and Theranostics Laboratory, Baker Heart and Diabetes Institute, Melbourne, Australia
[k] School of Environment and Science, Griffith University, Brisbane, Australia
[l] Australian Institute of Bioengineering and Nanotechnology, the University of Queensland, Brisbane, Australia

ARTICLE INFO

Keywords:
Thrombosis
Gold nanoparticle
Iron oxide nanoparticle
Photoacoustic Imaging
Magnetic resonance imaging
Photothermal therapy

ABSTRACT

Thrombosis is a major concern worldwide as thrombosis-related deaths are attributed to one in five deaths globally. Establishing a clot-targeting theranostic particle for diagnosis and treatment of thrombosis related diseases is crucial to provide rapid life-saving intervention. Herein, we developed activated platelet targeted gold-iron oxide nanoparticles (AuIONP) as a robust and powerful probe facilitating triple imaging modalities, including magnetic resonance imaging (MRI), photoacoustic imaging (PAI), and fluorescence imaging (FLI). Additionally, the antibody tagged AuIONP was utilised to facilitate photothermal thrombolysis, stimulated by the exposure to near-infrared (NIR) laser at 808 nm. In vivo observation of the targeted AuIONP showed a significant increase in MRI T_2*-weighted contrast and up to 3-fold more prominent photoacoustic signal and fluorescence intensity compared to the non-targeted group. Upon exposure to NIR laser at 1.5 W/cm^2, the localised temperature increase at the clot was observed in the targeted AuIONP treated group, facilitating a significantly higher reduction of thrombus area compared to the non-targeted treated group. Our work offers an innovative theranostic probe with excellent triple modality imaging and thrombolysis.

1. Introduction

Thrombosis is a condition in which the formation of a blood clot or thrombus occurs inside the blood vessel. Thrombosis-related diseases are the leading cause of mortality worldwide, estimated at one in four deaths [1]. This high prevalence of fatality is mainly due to the catastrophic effect of thrombosis on vital organs such as the heart and brain, causing life-threatening diseases such as heart attack and stroke [2,3]. Furthermore, one-third of COVID-19-related deaths is due to thromboembolism [4]. Concerns were also raised with COVID-19 vaccines as they show thrombogenic tendencies, leading to a few thrombosis-related deaths post-vaccination [5].

Severe thrombotic events are treated clinically with percutaneous coronary intervention procedures such as coronary angioplasty and thrombectomy [6,7]. Due to the invasive nature of these approaches and the possibility of complications such as haemorrhage and reperfusion injury, therapeutical use of thrombolytics are often preferred [8,9]. However, current thrombolytics approaches also have significant limitations. Age of thrombus is a crucial factor to determine prior to choosing treatment, with thrombolytics having higher success rate in

* Corresponding authors.
E-mail addresses: nghia.truong@monash.edu (N.P. Truong), h.ta@griffith.edu.au (H.T. Ta).

https://doi.org/10.1016/j.apmt.2023.101750
Received 22 August 2022; Received in revised form 14 November 2022; Accepted 26 January 2023

fresh thrombus as older thrombus is increasingly difficult and more resistant to the therapy [10]. Additionally, thrombolytic agents such as tissue plasminogen activator (tPA) and urokinase can cause an increase in bleeding risks, severely restricting their use [11].

As an alternative strategy, thrombus ablation could improve thrombolysis rate, such as the incorporation of nanoparticle-assisted photothermal therapy (PTT). In PTT, gold nanoparticle (AuNP) has been used to convert photo energy to heat which induces hyperthermia effect on thrombolysis [12]. Hyperthermia has been shown to disrupt fibrin strands, facilitating the process of blot lysis [13,14]. Additionally, AuNP can be tailored to absorb energy in the near-infrared (NIR) wavelength, the desirable range for PTT therapy due to their deep penetration through bodily fluid and tissues, providing a strong hyperthermia effect [15]. Furthermore, due to their unique optical and chemical properties AuNP has been widely documented as a promising probe for bioimaging in cardiovascular diseases [16]. These attractive features for both therapeutic and bioimaging, allows AuNP to be developed as a theranostic agent.

Theranostic approaches have continuously been developed and provide considerable value in achieving safer and more efficient diagnostic and therapeutic methods. On top of appropriate and patient orientated treatment, diagnosis of the disease is crucial in enabling a much faster response to thrombotic events [17]. Ultimately, accurate diagnosis with fast reliable approach is necessary in ensuring the provision of correct therapy for patients with thrombosis. One of the strategies to reduce this fatal incidence of thrombosis is to use sensitive and non-invasive methods to detect the formation of blood clots. However, most clinical diagnosis of thrombosis such as deep vein thrombosis is often unreliable and utilises time-consuming, low specificity laboratory screening tests such as D-dimer analysis [18].

Recently, non-invasive imaging modalities have been employed to observe ischaemic conditions in patients. Of these methods, magnetic resonance imaging (MRI) is widely used because of the depth of MRI images and the ability to quantify occlusive thrombosis [19]. Hyperdense vessels with signal abnormalities and the absence of normal blood flow can also be detected by MRI. Additionally, T_2* weighted gradient echo (GRE) imaging is beneficial for acute thrombosis, as significant magnetic susceptibility differences can clearly be observed due to the presence of deoxyhemoglobin [19]. Furthermore, MRI can be utilised to detect acute infarct due to the ability in distinguishing different wall thickness of the heart and the presence of oedema which produces shortening for T_2-weighted images [20]. However, longer acquisition time, limited availability, poor signal to noise ratio and resolution of MRI results still exhibit limitations in providing clear image analysis, which potentially can be resolved by other imaging techniques.

Fluorescence imaging (FLI) and photoacoustic imaging (PAI) are two other powerful diagnostic modalities in cardiovascular diseases, not only limited to imaging but has been utilised in assisting surgical procedures [21]. Comparatively easy and fast acquisition times are attractive features of both modalities [22,23]. However, each of these modalities cannot provide a comprehensive overview of the acquired images due to its inherent limitations, such as shallow tissue penetration depth, poor detection sensitivity, low spatial resolution, harmful ionizing radiation, slow imaging speed, inaccuracy, and/or high cost [23]. The combination of two or more imaging modalities would complement each other. For example, the combination of FLI and PAI would provide better depth and spatial resolution with better contrast especially towards tissue in atherosclerotic plaque compared to other techniques. Importantly, PAI and FLI may complement the strength of MRI to provide not only good depth and high spatial resolution but also compositional information [24,25]. Despite significant potential benefits, theranostic approaches with multi-modality imaging function to detect and image thrombosis are more sophisticated by design and present challenges that requires improvement and therefore are still urgently in need.

To this end, we aimed to develop the first hybrid gold and iron nanoparticle theranostic agent (AuIONP) with triple modalities by combining Au with iron oxide, a strong T_2* shortening contrast agent [26–34], and a fluorescent dye, Cy5 to provide multiple modality imaging for thrombosis with MRI, PAI and FI techniques. The AuIONP theranostic agent is also conjugated with scFv-SCE5, a single-chain antibody that can specifically bind to glycoprotein IIb/IIIa (GP IIb/IIIa) [35–37]. GP IIb/IIIa is the most abundant receptor on the surface of platelets, which mediates the process of platelet activation [38]. Data obtained from in-vitro and in-vivo experiments demonstrated that our novel AuNP theranostic agent could target blood clots, provide enhanced imaging, partially restore blood flow and open the blood vessel lumen.

2. Materials and methods

A comprehensive and extended version of the materials and methods section can be found in the Supplementary Materials section.

2.1. Synthesis and characterisation of PEGSH-AuIONP

Gold coated iron oxide (AuIONP) was prepared using a seeding method, which was modified from Ma *et al.* [39]. In brief, a solution of citrate-coated iron oxide (IONP) was mixed with hydroxylamine, trisodium citrate, and sodium hydroxide solutions prior to the drop by drop addition of $HAuCl_4$. The solution was allowed to stir and seed properly until a gradual change in colour from yellowish orange to green/bluish brown was observed. Dense gold-coated iron oxide particles were collected by centrifugation and dialysed overnight to remove unreacted components. To increase stability and introduce a functional group for specific targeting, coating with mPEGSH (MW: 6000 g/mol) and COOH-PEGSH (MW: 7500 g/mol) was established by incubating the whole solution overnight before purification by centrifugation.

2.2. Conjugation of scFv-N_3 and Cy5 to PEGSH-AuIONP

Prior to conjugation, scFv-N_3 was prepared following a similar protocol that was previously reported [40]. A more detailed protocol for the conjugation of scFv and Cy5 to PEGSH-AuIONP can be found in the supplementary section, with Fig. 3A summarising the overall procedures of the reaction. In short, scFv-SCE5 ($scFv_{Targ}$) and $scFv_{NonTarg}$ were coupled to an azide containing molecule (G-N_3) by sortase mediated ligation (SML). Meanwhile, dibenzylcyclooctane (DBCO) molecule and Cy 5 were introduced to PEGSH-AuIONP by 1-(3-dimethylaminopropyl)−3-ethyl carbodiimide (EDC) coupling reaction in MES buffer. For optimal DBCO and Cy5 conjugation, the reaction was maintained at 37 °C for overnight reaction, and followed by centrifugation to ensure elimination of unreacted components. scFv was added to the DBCO-AuIONP overnight reaction, and the resulting purified scFv-AuIONP was dispersed in PBS 7.4 and stored in 4 °C until further use.

2.3. In vitro human thrombus adhesion

Blood collected from blood bank (Red Cross Australia) was centrifuged at 1000 rpm for 10 min to collect the platelet rich plasma (PRP). Into a microcentrifuge tube 100 μL of the collected PRP was inserted and then incubated with 8.8 μL Actin (Siemens, Dade), and 2.5 μL of $CaCl_2$ 1 M for 30 min to create a firm platelet clot in a 37 °C incubator. To wash the clots, 1 ml of PBS pH 7.4 was added and maintained under rotation at 50 rpm for 30 min at room temperature. The clots were then incubated with the nanoparticles for 15 min at room temperature and 50 rpm rotation, followed by washing the unbinding nanoparticles extensively with PBS 7.4 and stored in 4% paraformaldehyde (PFA) solution.

For fluorescence imaging, the clots were placed inside a 24 well-plate and images were obtained using a Cy5 detection wavelength (excitation: 610 nm and emission: 680 nm) with Sapphire Biomolecular Imager

(Azure Biosystem). The images were collected in a 16-bit Tiff format and analysed with ImageJ. The clots were then embedded into a 50 ml microcentrifuge tube containing 1% agarose (Sigma Aldrich). MRI images were obtained using a 9.4T scanner (Bruker) with parameters TR = 2500 ms, TE = 60 ms, slice thickness = 1 mm, flip angle = 25. Images were analysed for maximum and minimum grey values using ImageJ and signal to noise ratio was calculated.

For photoacoustic imaging, the clots were created as described in the protocol above and stored in 4% para-formaldehyde (PFA) until imaging with Vevo LAZR instrument. The clots were placed in an ultrasound gel bed, ensuring no bubble was present near the clots. Image acquisitions were conducted with 30 MHz and gain value of 20 dB with step size of 0.92 mm. The images were analysed using the Vevo Lazr software with data demonstrating the percentage of photoacoustic signal as representation of photoacoustic signal intensity.

2.4. In vitro thrombolysis

Clots were prepared as described above. Into a 1.5 mL tube, 190 μL of PRP was added with 10 μL of red blood cells (RBC). Additionally, Actin (Siemens Dade) 17.6 μL and 2.5 μL of $CaCl_2$ 1 M (Sigma-Aldrich) were added to create a firm clot. The clots were incubated in a 37 °C incubator and washed thoroughly with PBS afterwards. The clots were weighed (W_0) and various variables including laser intensity strength, exposure time, Au concentration and cycles were applied. The 808 nm laser (Eforce Laser) was maintained at a distance of 10 cm from the clot, to ensure a 1 cm^2 laser diameter, and the final weight of clot (W_a) was measured after treatment. Near infrared thermal images were also obtained prior and after laser treatment to observe the change in temperature with an infrared thermal camera (FLIR C2). The supernatant of the solution was collected, centrifuged at 1000 g and the optical density was read at 545 nm. The percentage of lysis was calculated based on the reduction of the weight of the clots.

2.5. In vivo imaging

In vivo experiments were conducted at Centre of Advanced Imaging, The University of Queensland (Brisbane, Australia). All animal care and experimental protocols have been approved by The University of Queensland Ethics Committee (No. AIBN/420/19/CAI) and all procedures were carried out in accordance with the approved protocols. For the experiment, 11 to 12 weeks old C57/BL6 mice (Animal Resources Centre, ARC. Western Australia) weighing around 24–28 g were anaesthetised with a mixture of ketamine:xylazine (dose of 100:10 mg/kg body weight) by intraperitoneal injection. Fur covering area around the chin, arm and stomach were gently removed using a hair removal cream (Veet) and the applied area was cleansed from cream residue with water thoroughly. In order to induce arterial thrombosis, a small Whatman filter paper (1 × 3 mm) was immersed in $AlCl_3$ 9% and placed on the isolated left carotid artery for 2 min. After application, the area was cleaned thoroughly with saline, and the isolated artery was inserted back inside the body. Tail vein catheterisation was performed to facilitate sample injection during imaging 10 min post injury.

Two different groups were analysed for both imaging and thrombolysis, which were mice injected with targeted AuIONP group and mice injected with non-targeted AuIONP group. For MRI imaging, the mice were placed into the MRI system (Bruker), which comprised of 23 mm internal diameter mouse head coil. Anaesthesia was maintained with 0.5–1% of isoflurane in oxygen and vital signs were monitored throughout the imaging by observing breathing rate monitor which was connected to the mousebed. Scanning localiser images were taken to acquire coronal, sagittal and transversal images in the correct position, with parameters as follows: TR = 1600 ms, TE = 32 ms, slice thickness = 0. 6 mm, flip angle = 180°, pixel bandwidth = 238 Hz/Px and acquisition matrix of 256 × 138. 2D T2* weighted gradient echo images were acquired at baseline with parameters that were utilised during the acquisition as follows: TR = 500 ms, TE = 4.58 ms, slice thickness = 0.4 mm, flip angle = 35°, pixel bandwidth = 260 Hz/Px and acquisition matrix of 192 × 192.

After baseline, AuIONP was injected with a dose 6.5 mg/kg body weight (composed of 328 μg Fe/kg body weight and 3.08 mg Au/kg body weight based on ICP result). Images were obtained every 15 min post injection until 60 min. Change in intensity around the region of interest (ROI) were analysed after data acquisition using ImageJ by comparing signal observed after injections (Sn) and before injection or baseline (S_0). The targeted AuIONP data was compared with the non-targeted AuIONP data to observe the targeting effect of AuIONP.

Photoacoustic imaging was taken immediately after the MRI image acquisition using MSOT system (inVision 256TF, iThera Medical). Previous spectra of the AuIONP was loaded into the spectral analysis along with haemoglobin (Hb) and deoxygenated haemoglobin (HbO_2). The mouse was placed in a thin layer of plastic wrap with ultrasound gel covering the neck area to ensure no air pockets were present. Then the mice was inserted into the water chamber of the MSOT and images were obtained for the area near the incision on the neck. Images were taken on multiple wavelengths ranging from 680 to 980 nm with slices every 0.2 mm. Obtained images were further reconstructed with the MSOT software and overlayed with the spectral profiles of the AuIONP, Hb and HbO_2. Mean pixel intensity of the ROI was analysed using the MSOT software and compared between targeted and non-targeted group.

Fluorescence imaging was obtained using the IVIS System (Lumina S5, Perkin Elmer). Mouse was placed on top of the platform inside the system and was adjusted to a distance of 10 cm from the camera until the area of interest was visible. Fluorescence imaging was selected with Cy 5 emission and excitation at 620 and 650 nm respectively. Images were taken at baseline, 5 min and every 15 min until 1 hour after injection of the nanoparticles. Fluorescence intensity and total radiant efficient were analysed using the IVIS software. All animals during the imaging were maintained under anaesthesia with a flow of isoflurane of 1–2% with oxygen flow of 1–2 L/min.

2.6. In vivo thrombolysis

Blood flow in the clotted vessel was observed using a 0.5 mm flowmeter probe (Transonic) and the flow reading was observed at 160 Hz for 5 min. The clot area was irradiated by the 808 nm laser at 1.5 W/cm^2 for 3 min and was rested for 5 min before being exposed with two more cycles of laser treatment. Temperature before and after laser was obtained using infrared thermal camera (FLIR C2). Observation of the change in blood flow was measured again 30 min after the last laser exposure, and the change in maximum and minimum flow value was calculated between the targeted and non-targeted group. After thrombolysis observation was completed, the mice were maintained under deep anaesthesia with isoflurane, and the clotted section of the carotid artery was collected, washed with PBS and fixed with 4% PFA. The collected carotid arteries were then processed with an Optical Coherence Tomography (OCT) at 4 °C, frozen with dry ice, prior to sectioning with a thickness of 10 μm, and further stained using Masson Trichrome. The prepared histological slides were observed under brightfield microscope (Olympus) and analysed for thrombus area.

2.7. Statistical analysis

All the values provided are shown in mean ± standard deviation (SD), unless otherwise indicated. Data were analysed for statistical significance using one-way ANOVA and Tukey multiple comparison test (Graphpad Prism 8), with * $P < 0.05$ considered significant while ** $P < 0.01$, *** $P < 0.001$, and **** $P < 0.0001$ to be very significant.

3. Results and discussion

3.1. Preparation and characterisation of AuIONP

We designed and synthesized the nanotheranostic agent composed of gold, iron oxide and a single-chain antibody (scFv) for diagnosis of thrombosis by utilising MRI, FI and PAI, while simultaneously possessing the ability to induce photothermal thrombolysis. The general scheme of the nanoparticle synthesis can be seen in Fig. 1A. Briefly, AuNPs were seeded on the surface of iron oxide nanoparticles, followed by the process of PEGylation for improving particle stabilisation. To introduce targeting ability to the nanotheranostic agent, PEG is also used as a functional group to conjugate with scFv. Particularly, citrate capped iron oxide nanoparticles (IONP) were first synthesised using a seeding method that was developed to increase the T_2 relaxivity of iron oxide [41]. It was documented that aggregates or cluster of IONP significantly presents higher transverse relaxivity compared to single IONP thereby increasing the efficiency of IONP as a T_2 weighted contrast for MRI [42]. Cluster shaped IONP can be seen from the TEM in Figure S1 (see: supplementary materials). Although the IONPs do not have a spherical shape, characterization of the IONP by dynamic light scattering (DLS) showed a hydrodynamic volume (Z average size) of 47.9 ± 0.2 nm, polydispersity (PDI) of 0.234 ± 0.004, and zeta potential of −26.0 ± 1.2 mV.

In order to produce nanoparticles with desired near-infrared absorbence (NIR), we next coated AuNPs on IONPs to form AuIONPs. The AuIONPs purposely-designed to be asymmetric, creating a nanostructure resembling a rosette (nanorose AuIONP). The obtained solution of AuIONP was dark with a tinge of bluish-green in colour (Fig. 1F), with an average size of 80.5 ± 0.3 nm, PDI of 0.265 ± 0.016 and zeta potential of −28.92 ± - 0.84 mV (Table 1). The asymmetrical shape and the size of ~100 nm facilitated the strong absorbence observed in the NIR range with a peak of around 780 nm (Fig. 1C). A line indicating 808 nm was drawn on the graph to indicate the intensity present at 808 nm which correlates with the laser wavelength that is utilised for photothermal induction in this study. TEM image confirms the nanorose shape of AuIONP with knobby protrusion (Fig. 1D) and a size of ~100 nm. From our TEM images we were unable to conclusively confirm whether AuIONP is composed from a single iron oxide or a cluster, due to the low percentage of Fe in AuIONP. However, from both ICP and energy-

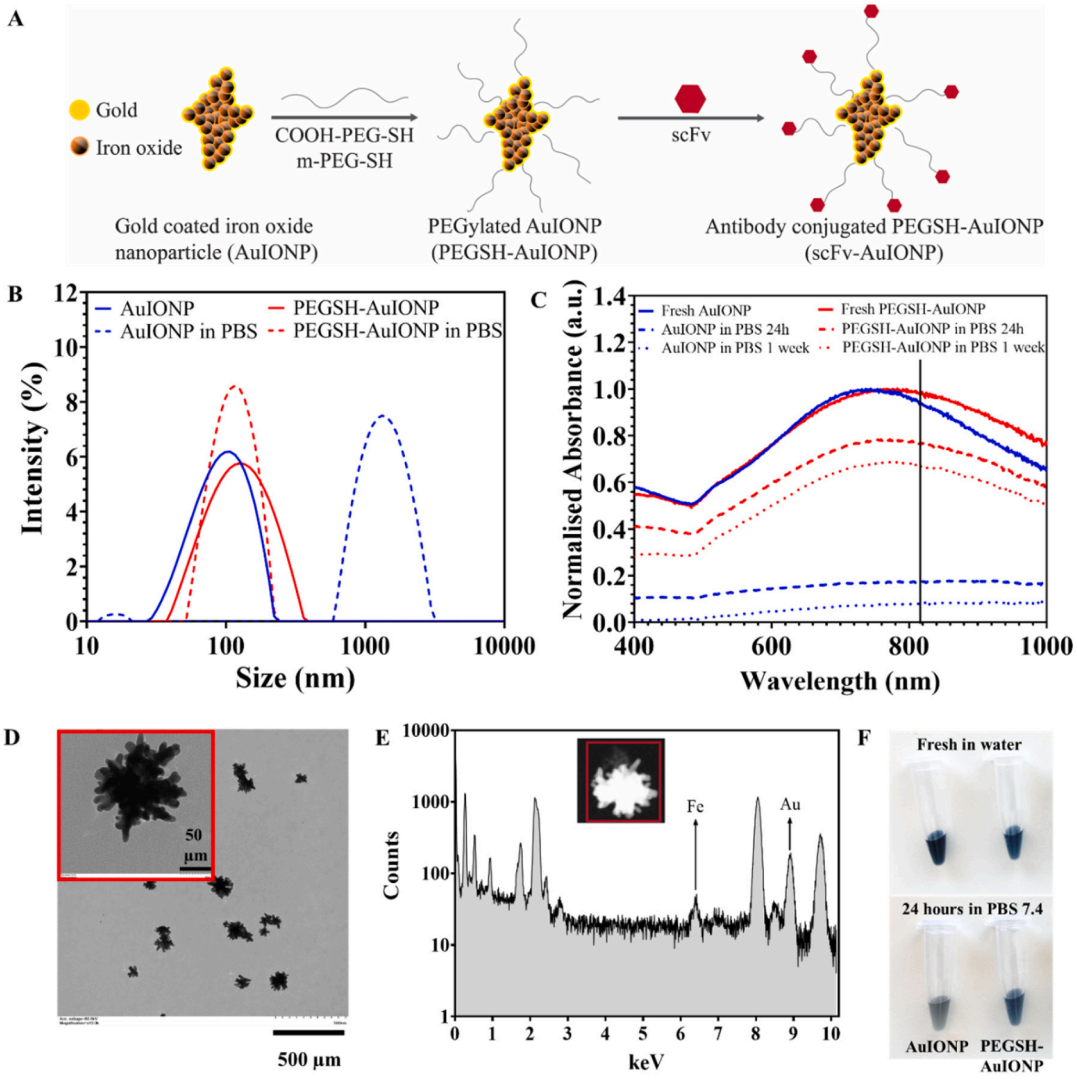

Fig. 1. Synthesis and characterisation of AuIONP (A) Schematic diagram of AuIONP to scFv-AuIONP synthesis. (B) The size distribution of AuIONP (blue line) and PEGSH-AuIONP (red line) by dynamic light scattering before (non-dotted line) and after incubation in PBS (dotted line). (C) absorbence spectra of AuIONP and PEGSH-AuIONP before and at multiple time points after incubation in PBS (D) TEM image of the AuIONP displaying nanorose structure. (E) EDS spectra indicating the presence of elemental Au and Fe. Insert displaying the shape of the AuIONP that was analysed. (F) Photographs taken of uncoated AuIONP (left) and PEGSH-AuIONP (right), before (top) and after incubation in PBS (bottom).

Table 1
Particle characterisation of AuIONP ($n = 3$).

Samples	In Water			In PBS 24 h later	
	Z-average (nm)	**PDI**	**Zeta Potential (mV)**	**Z-average (nm)**	**PDI**
AuIONP	80.5 ± 0.3	0.265 ± 0.016	−28.92 ± -0.84	1426.2 ± 302.3	0.176 ± 0.035
PEGSH-AuIONP	119.7 ± 1.8	0.201 ± 0.023	−24.77 ± -0.37	111.1 ± 2.7	0.149 ± 0.020
DBCO-AuIONP	147.6 ± 2.1	0.210 ± 0.077	−21.38 ± 0.92		
scFv-AuIONP	197.5 ± 7.5	0.262 ± 0.022	−14.43 ± 0.61		

dispersive x-ray spectroscopy (EDS) results, we conclusively confirmed the presence of both Au and Fe in the system, with characteristic x-ray peaks of Au and Fe at ~9.7 and ~6.4 keV, respectively (Fig. 1E) [43].

Despite citrate coating being able to stabilise AuIONP by electrostatic repulsion, the nanoparticles were not stable enough in physiological buffers [44,45]. To improve the particle stability, thiolated-PEG was introduced to AuIONP by ligand exchange and a PEG coating was readily established due to the strong thiolate-Au (SH-Au) bond (binding energy of 40–50 kcal/mol compared to only 2 kcal/mol of Au-COOH) [46]. We combined two types of PEG, carboxylic-PEG-thiol (COOH--PEG-SH) and methoxy-PEG-thiol (mPEG-SH), to provide a COOH functional group for further modification with scFv on the surface of the particles. The hydrodynamic volume of the PEG-coated AuIONP increased to ~119 nm, suggesting the successful PEG coating (Fig. 1B). Additionally, PEGylated AuIONP (PEGSH-AuIONP) was stable in phosphate buffer saline (PBS) pH 7.4 for 24 h, evident by unchanged particle size (Fig. 1B, Table 1) and relatively similar absorbence intensity (Fig. 1C).

After synthesis, we characterized the properties of the PEGSH-AuIONP. Images from T_2* weighted MRI 7T scans showed the enhanced T_2* weighted signal of PEGSH-AuIONP in a Fe concentration-dependant manner (Fig. 2A). The transversal relaxivity (R_2*) obtained with PEGSH-AuIONP was lower than the R_2* measured in Antal *et al.* (2020) result, with 61.3 and 285.8 $mM^{-1}.s^{-1}$ respectively (Fig. 2C) [40, 47]. This was expected due to the additional Au and PEG layer on PEGSH-AuIONP that is present in our system as compared to the pure uncoated IONP in previous research. Brennan et al. [48] noted the influence of gold shell thickness on IONP which exponentially reduced the relaxivity for both T1 and T2 as well as magnetophoresis rate and magnetic induced hyperthermia. Despite the limitation, the value of R_2* that was generated by the AuIONP system is still sufficiently high in comparison with biological structures to provide diagnosis in detecting abnormalities within blood vessels or biological tissues [49].

As previously described, the additional advantage of AuIONP system is the ability to provide multimodality imaging. Au is a versatile material which can be tailored to be photoacoustically active, with nanorod and nanostar or nanorose AuNP structures providing the most optimally high photoacoustic signal [50,51]. In this instance, AuIONP photoacoustic signal was observed with the increase in the obtained mean pixel intensity (MPI) of the PEGSH-AuIONP (Fig. 2B). The trend of MPI increase also indicated a concentration-dependant occurrence (Fig. 2D). From the wavelength versus MPI spectral analysis, we can conclude that PEGSH-AuIONP demonstrated the strongest photoacoustic signal at 680 nm (Fig. 2E), which is within the ideal photoacoustic window for deep tissue imaging with minimal interference from biological structures and components [51,52].The difference between absorption and photoacoustic wavelength peak of AuIONP can be explained based on the underlying difference in mechanism of how these spectra were gathered. absorbence signal relies on the amount of optical absorption by the particle, meanwhile photoacoustic signal interprets the amount of pressure that propagates (acoustic wave) through the sample due to the thermoelastic expansion generated by the heat that was converted from optical absorption [53]. Other studies have also reported this difference of absorption and photoacoustic spectra phenomenon [54,55].

3.2. *Conjugation with Cy5 and scFv (activated platelet targeting antibody)*

In this study, we employed a single-chain antibody with known specific binding to activated platelets ($scFv_{SCE5}$), specifically on the activated form of the integrin GPIIb/IIIa. The higher affinity of $scFv_{SCE5}$ will allow the system to be more robust in targeting thrombi, even in

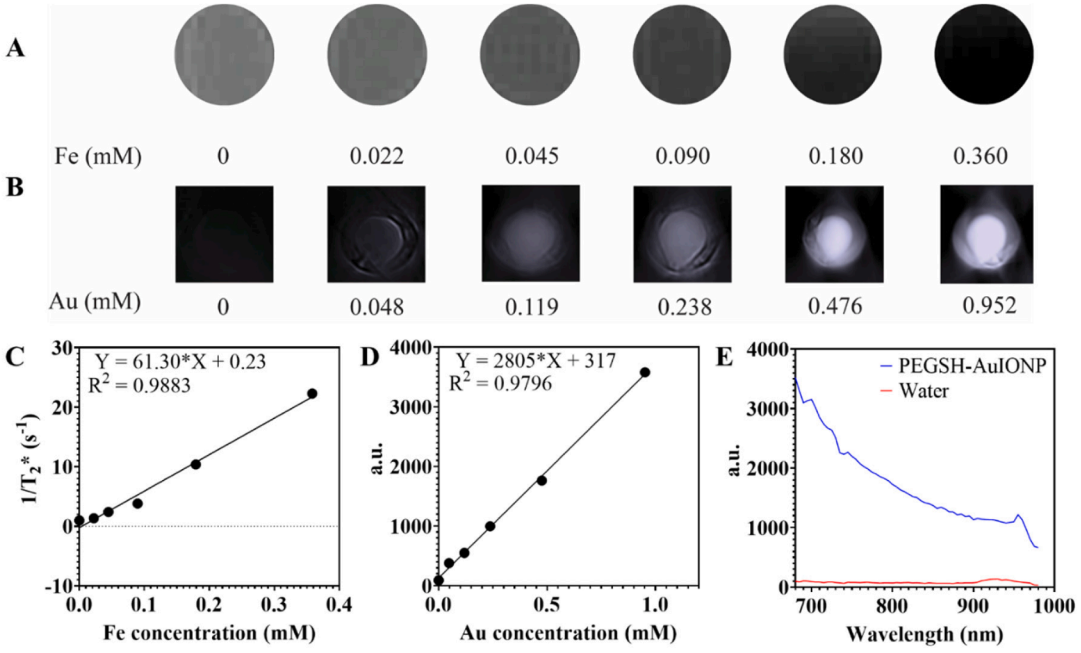

Fig. 2. In vitro MRI and photoacoustic images of PEGSH-AuIONP (A) MRI T_2 weighted and (B) photoacoustic images of PEGSH in phantom. (C) Relaxivity (R_2) of T_2* weighted results of PEGSH-AuIONP, (D) Correlation between concentration of Au and MPI at 680 nm and (E) Photoacoustic spectra of PEGSH-AuIONP and water.

situation where the thrombi possess low number of platelets, such as in venous thrombosis [40,56]. To perform the conjugation, sortase-mediated ligation (SML) was first used to ligate the C terminus of scFv SCE-5-LPETG to an azide (N_3) containing peptide (Fig. 3A step 1). The protocol used in this study was modified from Ta et al. [40,57] which had successfully applied the method for similar antibody and peptide. Successful conjugation of the N_3 to the scFv was confirmed by the SDS-PAGE gel showing the change in molecular weight of the resulting conjugated $scFv^{Targ}$-N_3 (lane 2 Fig. 3D) that was smaller than the control $scFv^{Targ}$ (lane 1 Fig. 3D). This is due to the small size of the azide molecule (0.27 kDa) and the loss of LPETG tag during the sortase reaction [36]. Based on SDS-PAGE and BCA assay, the obtained reaction yields were 74 and 78% respectively, which is considered sufficiently high despite a comparably lower yield than the result from Ta *et al.* due to the difference in the purification process [40]. Similar steps were applied to the $scFv^{Nontarg}$, a non-platelet binding mutated variant of the scFv, with changes in $scFv^{Nontarg}$-N3 size (Fig. 3D lane 3 and 4), therefore demonstrating that N_3 was also successfully introduced.

Subsequently, the obtained PEGSH-AuIONP were further modified with Cy5, a fluorescent molecule and DBCO to facilitate copper-free click chemistry reaction with the N_3 present on the scFv obtained after SML. The coupling between COOH on PEGSH-AuIONP and the NH_2 present on Cy5 and DBCO was performed using EDC (Fig. 3A step 2). The obtained nanoparticle (DBCO-AuIONP) was analysed with DLS, which indicates the increase in particle size to around 147 nm with a lower negative zeta potential value, demonstrating a reduced number of free

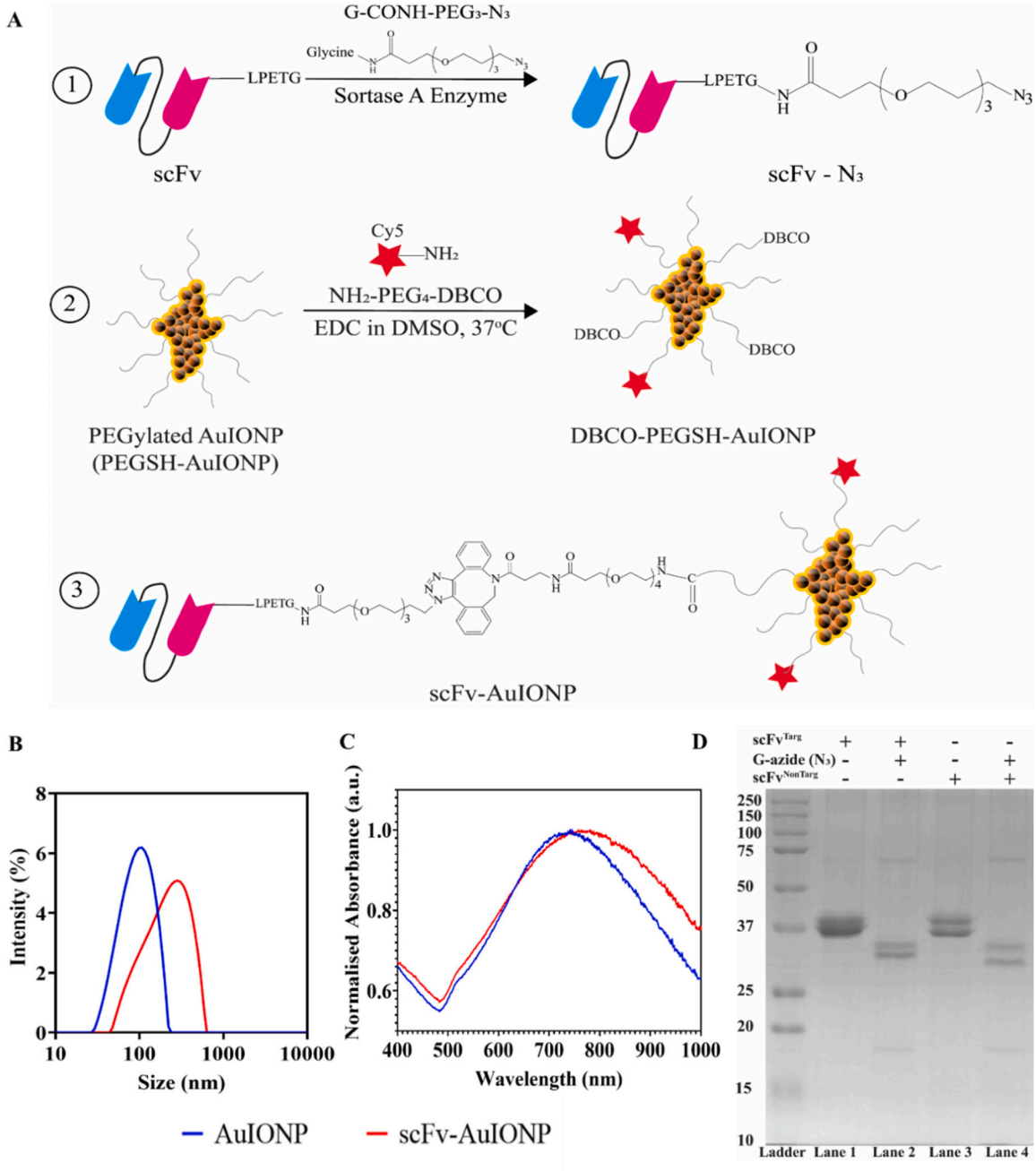

Fig. 3. Conjugation Analysis of PEGSH-AuIONP with Cy5 and scFv. (A step 1) Schematic diagram of SML ligation of scFv to G-azide; (A step 2) PEG-AuIONP with DBCO and Cy5 and (A step 3) The final construct of scFv-AuIONP post click reaction between the DBCO conjugated PEG-AuIONP and the scFv-azide. (B) Size distribution comparison of AuIONP and scFv-AuIONP. (C) absorbence spectra of AuIONP and scFv-AuIONP (D) SDS-PAGE SML results of $scFv^{Targ}$ and $scFv^{NonTarg}$ with azide.

COOH groups due to established conjugation of Cy5 and DBCO (Figure S2,Table 1). Labelling of PEGSH-AuIONP with Cy5 was further evaluated by measuring fluorescence intensity using a microplate reader (Figure S2B) and imaging with Sapphire imager system (inset images). As shown by the fluorescence intensity, Cy5 was successfully conjugated to the PEGSH-AuIONP. Despite the confirmed conjugation, the fluorescence intensity was influenced by the AuIONP, as AuNPs are notably one of the most efficient quenchers of fluorescence [58].

The final step of the conjugation is coupling the N_3 tagged scFv with the DBCO-AuIONP, through strain promoted alkyne-azide cycloaddition (SPAAC) reaction (Fig. 3A step 3). This method allows site-specific conjugation of scFv on the surface of the AuIONP while preserving the antibody binding capacity [59]. Efficient binding of the scFv to AuIONP was obtained, and the percentages of conjugation by SDS-page and BCA assay were 76 and 62% of conjugation, respectively (Figure S3 and S4). This result was further supported by the increase in size and a decrease in charge of the scFv-AuIONP (red line in Fig. 3B and Table 1), due to the presence of free NH_2 on the scFv and the loss of free carboxylic groups after the conjugation [60]. Additionally, in a complementary analysis, agarose separation between PEGSH-AuIONP, and scFv-AuIONP showed the broader band of PEGSH-AuIONP demonstrating that scFv-AuIONP has a lower negative charge value when compared to PEGSH-AuIONP (Figure S5). Ultimately, the final collected scFv-AuIONP maintained strong absorbence in the NIR region (Fig. 3C) with desirable size and efficient scFv conjugation.

3.3. In vitro human thrombus adhesion assay

The adhesion of targeted NPs ($AuIONP^{(+)}$) and non-targeted NPs ($AuIONP^{(-)}$) with thrombus created from human platelet was analysed using several techniques. MRI, photoacoustic and fluorescence imaging results showed specific binding of the $AuIONP^{(+)}$ with a more prominent signal as compared to $AuIONP^{(-)}$ (Fig. 4A, 4B and 4C). Moreover, as can be seen in the images and the signal analysis comparison, the binding also showcased a concentration dependant effect, with more particles binding to the thrombus in the higher concentration group. Significantly higher photoacoustic percentage signal, grey value (T_2* contrast darkening effect) and fluorescence intensity were recorded in the $AuIONP^{(+)}$ treated groups (Fig. 4D, 4E, and 4F). These in vitro results demonstrated the ability of $AuIONP^{(+)}$ to specifically bind to the human thrombus.

To further prove the binding ability of $AuIONP^{(+)}$ to human activated platelets, the particles which tagged with Cy5 were visually observed under flow condition of 1000 s^{-1} shear rate in a microfluidic device [61]. The shear rate of 1000 s^{-1} mimics the pulsatile flow condition typically found in arteries with a pathological condition such as atherosclerosis [62]. The microfluidic polydimethylsiloxane (PDMS) based device was specifically designed as an *in-vitro* device for atherothrombosis related studies and applications. Platelets that were stained with DiOC6 dye (bright green fluorescence in Fig. 4G), were infused through the channel for 10 min and formed a stable thrombus on the exposed collagen layer, which allowed for a better representation of the physiological condition of arterial thrombosis. The results showed that obtained $AuIONP^{(+)}$ had significantly higher binding to the platelet, as shown by the large area of red fluorescence signal, compared to the $AuIONP^{(-)}$. Moreover, increased binding can be observed over time, indicating the number of particles binding to the thrombus increased with time (Figure S6). The data gathered in these experiments provide the evidence that $AuIONP^{(+)}$ can specifically bind to activated platelets and thrombus.

3.4. In vitro thrombolysis on human thrombus

Prior to establishing the effect of laser towards thrombolysis, AuIONP ability to induce thermal increase was observed with an infrared camera. As can be observed in Fig. 5A, the presence of AuIONP with concentrations of 10 and 50 ppm were able to induce a temperature increase of up to 2-fold as compared to the control group (PBS solution with laser treatment alone). Various temperatures were reached with different laser intensities, with the lower 1 W/cm^2 exhibiting a final temperature of around 45 °C, while the highest intensity of 2 W/cm^2 reached as high as 58 °C. Due to their unique optical properties, Au is an ideal nanomaterial for photothermal sensitisers, which can generate heat by strong light absorption [63]. Additionally, the nanorose shape of AuIONP has a large surface area leading to intense heat generated on the surface of the particle which then was transferred to the surrounding solution [64,65]. Based on our calculation, the AuIONP photothermal conversion efficiency (η) value we obtained was 37.47% (Figure S7). This finding is comparatively lower than the reported η value of Au nanorods by Chen et al. with values ranging from 51-95% [66]. However, this result is expected due to the effect of size and particle volume of AuNP towards photothermal efficiency. Chen et al. demonstrated a decrease of photothermal efficiency up to 50% from Au nanorods when the particle radius increased from 10 to 50 nm [66]. Additionally, it is crucial to note that despite lower photothermal conversion efficiency value, it does not translate to poor or limited heat generation. As supported by a report from Qin et al. Au nanosphere with a size of 100 nm produced 150 times more heat than 15 nm size Au nanosphere despite 46% lower photothermal conversion efficiency [67].

In vitro thrombolytic efficacy of the AuIONP was evaluated by the change of thrombus weights after treatments. Artificial thrombus was first created by allowing the interaction of calcium chloride and Actin FSL. The presence of phospholipid from Actin FSL, will activate the intrinsic coagulation pathway and calcium ions facilitate the trigger for coagulation, ensuring a firm thrombus to form [68]. As shown in Fig. 5B. the changes in the thrombus and their weight were compared between the NIR 808 nm irradiation groups with different laser intensities. We also conducted testing with other variables, including exposure time, concentration, and number of cycles (Fig. 5). Consequently, varying degrees of lysis of blood clots could be observed in all the groups after different treatments.

From the variation of laser intensity, we observed significantly higher percentage of lysis occurring with the 2 W/cm^2, as compared to the lower intensity of 1 and 1.5 W/cm^2. Blood clots treated with laser visibly smaller and produced more intense red colour in the collected solution as compared to the PBS solution with laser treated group (Fig. 5C and 5D). As explained by Zheng et al. [14], haemolysis are expected to occur during thrombolysis, as RBC are significant constituents of a thrombus, therefore significant thrombus reduction requires the apoptosis of RBC present in the thrombus matrix. However, the temperature increase was exceedingly high and potentially unsafe for in vivo applications. Additionally, the longer exposure time of the laser also significantly increased the lysis and the temperature.

Interestingly, implementing off time between laser exposure prevented excessive temperature increase, hence allowing a relatively controlled temperature that is more suitable for thrombolysis. This is due to the reduction of temperature while the thrombus is not exposed during off time. From these promising findings, we further explored the optimum condition of 1.5 W/cm^2, exposure time of 3 min for 3 cycles for thrombosis in vivo application. In previous study, Singh et al. [12] utilised a solution of gold nanorod to achieve 16.3% of thrombolysis, after exposing fibrin clots with 808 nm laser and intensity of 1.05 W/cm^2 for 45 min. Compared to this result, we were able to obtain higher lysis in significantly shorter time with similar laser intensity.

3.5. In vivo MRI, PAI, and FI

The carotid arterial model of thrombosis has been extensively used in the small animal thrombosis model. $FeCl_3$ can induct thrombus but also trigger the release of free radicals leading to lipid peroxidation and endothelial cells damage [69]. In addition, $FeCl_3$ is known to create significant MRI artefacts, rendering it unusable in this study. Alternatively, $AlCl_3$ has been investigated and shown the ability to induce a

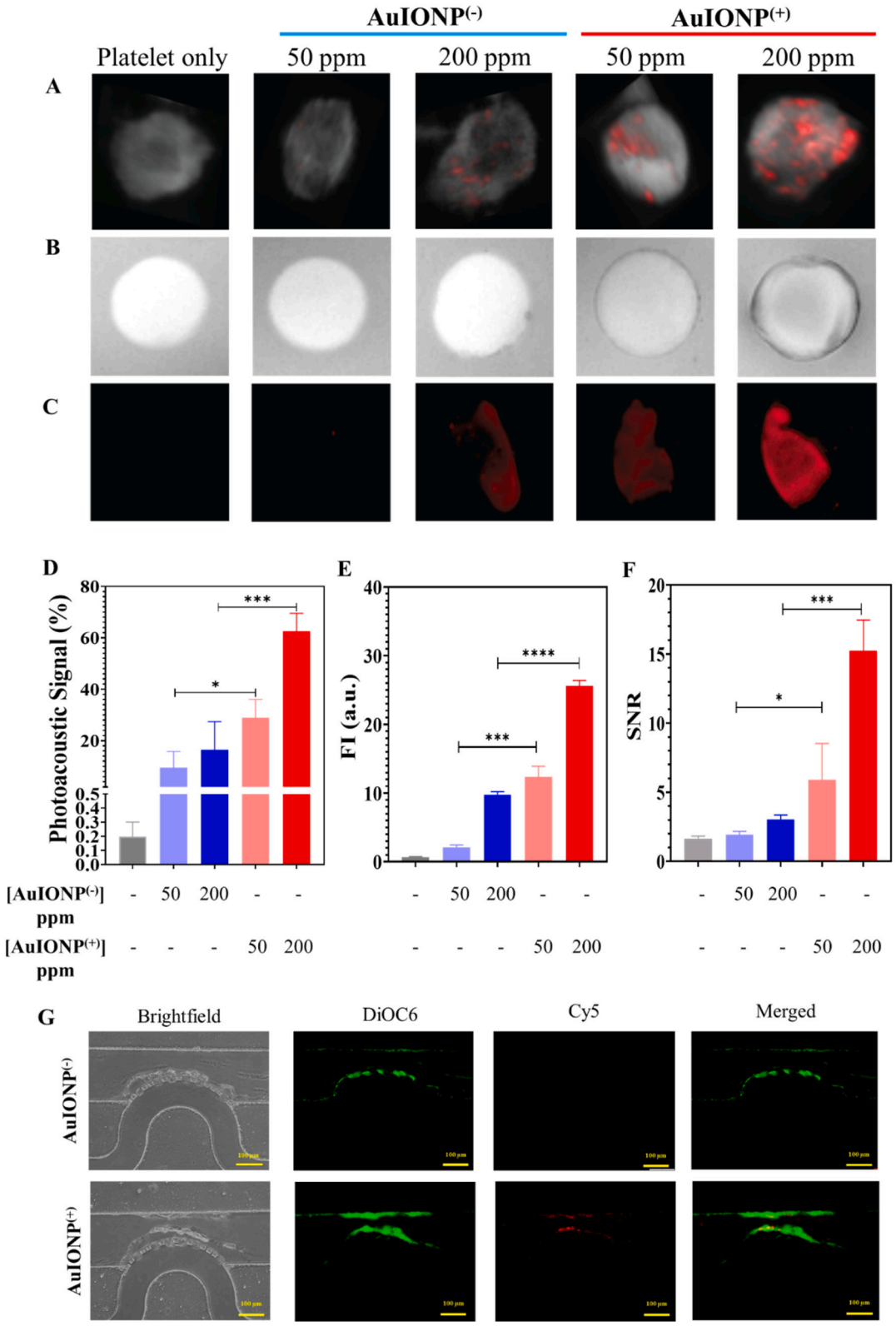

Fig. 4. In vitro human thrombus and activated platelet binding assay. (A) Photoacoustic signal observed on thrombus (red dots), with more apparent binding observed at the high concentration AuIONP$^{(+)}$. (B) MRI images of thrombus, more significant binding observed in targeted indicated by the black layer around the clots. (C) Fluorescence imaging at Cy5 emission range, a more intense fluorescence image was obtained with the targeted. (D) Analysis of photoacoustic signal indicating significant difference between AuIONP$^{(-)}$ and AuIONP$^{(+)}$. (E) Ratio analysis of grey images, maximum to minimum ratio indicating significant difference between AuIONP$^{(-)}$ and AuIONP$^{(+)}$. (F) Fluorescence intensity of the binding assay, with targeted group exhibiting significant difference compared to non-targeted. Statistical analysis was done with one-way ANOVA and Tukey multiple comparison test ($n = 3$; ns $p > 0.05$, * $P < 0.05$, ** $P < 0.01$, *** $P < 0.001$, and **** $P < 0.0001$) (G) Fluorescence images of the flow binding assay, with AuIONP$^{(+)}$ (red fluorescence) illustrating higher binding to the DiOC6 stained platelets (green fluorescence) compared to AuIONP$^{(-)}$ group (yellow scale bar =100 μm).

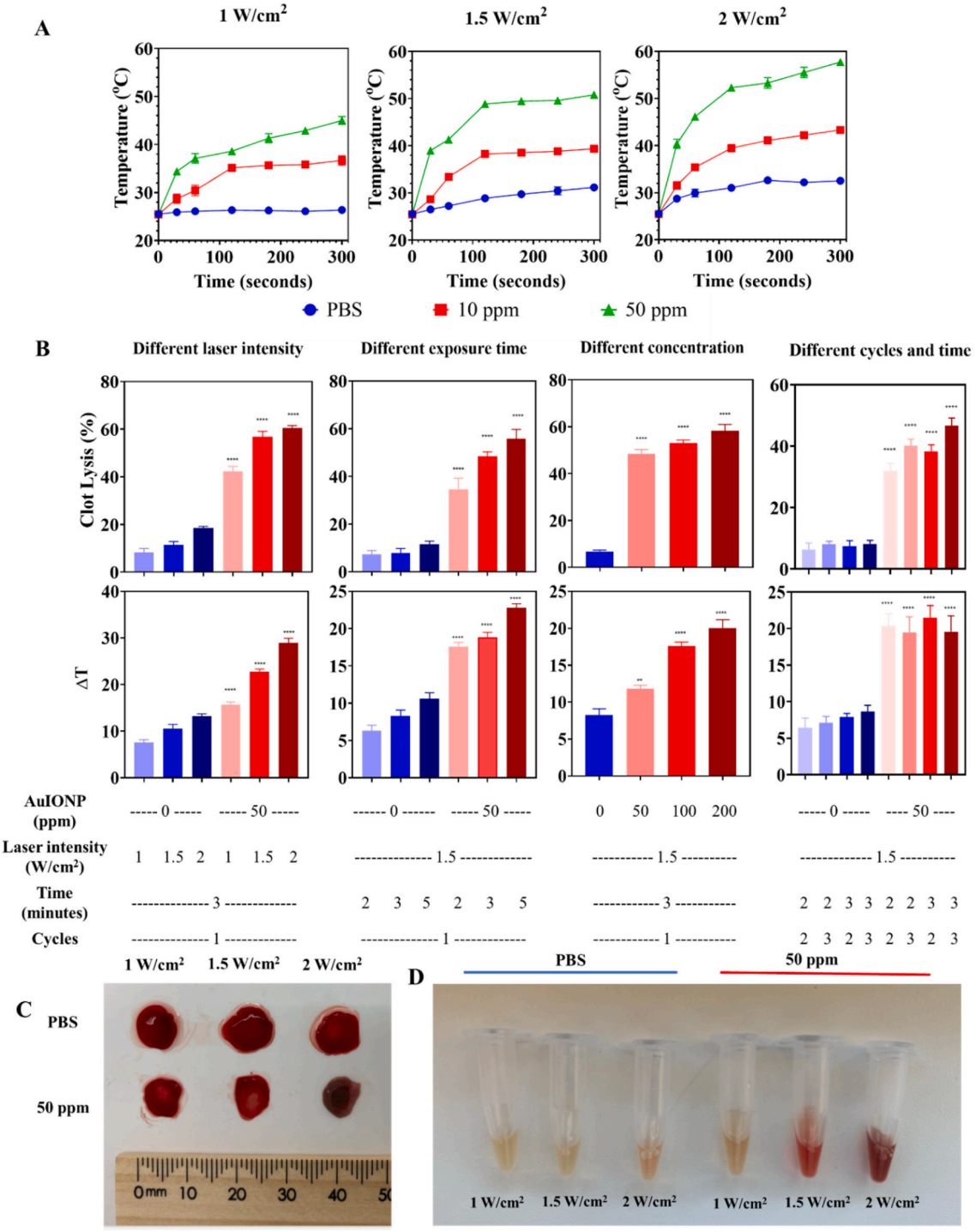

Fig. 5. In vitro photothermal properties and thrombolysis study. (A) Increase of temperature observed at specific time point with PBS, PEGSH-AuIONP at 10 and 40 ppm. (B) Percentage of clot lysis (top) and temperature increment (bottom) observed on thrombus ($n = 4$; ns $p > 0.05$, * $P < 0.05$, ** $P < 0.01$, *** $P < 0.001$, and **** $P < 0.0001$).. (C and D) Qualitative thrombolysis observed visually, with apparent reduction in size and increased haemolysis observed in the AuIONP treated clots with different laser intensity.

similar thrombogenic mechanism as $FeCl_3$ with no significant MRI artefacts [70]. In this study, we used $AlCl_3$ 9% to establish a stable thrombus in the left carotid artery.

In thrombosis MRI images were obtained with a 7T imaging system at different time points before and after injection. As can be seen in Fig. 6A, darkening of the thrombus area is more prominent in the AuIONP$^{(+)}$ group, while the AuIONP$^{(-)}$ showed negligible change. By comparing the ratio of grey value of baseline to the value at each time points, a ratio (Sn/S_0) was obtained. The significant change in the grey value can be seen, starting from 15 min post injection to 30 min post injection (Fig. 6D). However, there was no significant change from the 30 min to 60 min acquisition, indicating the binding of AuIONP$^{(+)}$ occured rapidly, within the first 30 min post injection. It was previously reported that scFv tagged IONP was able to produce a significant enhancement of T_2 shortening on the thrombus affected carotid arteries in 30 min, with a peak signal to noise ratio after 70 min, which signifies

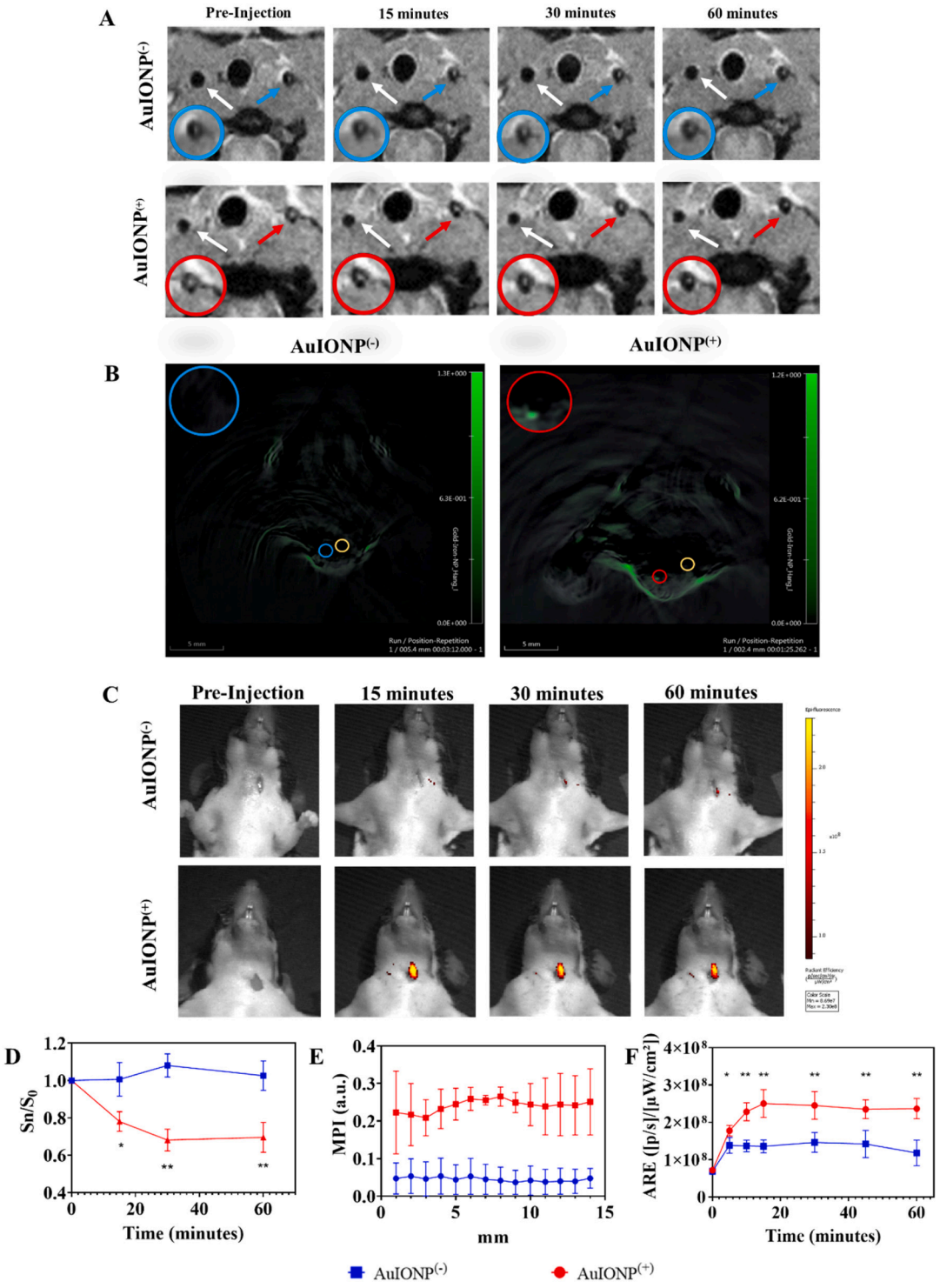

Fig. 6. In vivo MRI, PAI, and FLI. (A) In vivo MRI of carotid artery thrombus before and after administration of the nanoparticles at different time points. Blue arrows indicate the thrombus inside the left carotid artery in the AuIONP$^{(-)}$ group, while red arrows represent AuIONP$^{(+)}$ treated thrombus. The white arrows showing the non-occluded right carotid artery. Inset images inside the circles represent enlarged views of the left carotid artery emphasising on the change of contrast. (B) Photoacoustic images of AuIONP$^{(-)}$ and AuIONP$^{(+)}$ treated groups. Inset images on both (A) and (B) represents the enlarged images of the selected areas. (C) Fluorescence intensity observation of the carotid arteries. Mice that were injected with AuIONP$^{(+)}$ exhibited distinctly higher fluorescence signal. (D) Comparison of signal changes observed at different time points, blue and red lines represent the non-targeted and the targeted AuIONPs respectively. (E) Photoacoustic signal enhancement in AuIONP$^{(+)}$ treated groups, indicated by the higher mean pixel intensity (MPI) than non-targeted groups (F) Average radiant efficiency (ARE) observed plotted over time. Significant increase of ARE on the AuIONP$^{(+)}$ treated groups was observed as 5 min and peaked at 15 min after injection ($n = 4$; ns $p > 0.05$, * $P < 0.05$, ** $P < 0.01$).

that our AuIONP can produce just as strong signal enhancement with T_2* weighted MRI [40].

Similarly, MSOT imaging exhibited a stronger photoacoustic signal around the vessel of the AuIONP$^{(+)}$ group (red circle) as compared to the non-targeted group (blue circle) in Fig. 6B. From the image we can visualise the presence of a bright green photoacoustic signal in the AuIONP$^{(+)}$ group 60 min post injection, which indicated that the particles were able to accumulate on the thrombus sufficiently to enhance photoacoustic signal. The presence of AuIONP$^{(+)}$ increased the photoacoustic signal by almost 3-fold increase compared to the AuIONP$^{(-)}$ treated group (Fig. 6E). This 3-fold enhancement of signal intensity is comparable to a previous report utilising RGD tagged porphyrin-like mesoporous carbon nanostructures (PCMS), where they were able to observe an increase of around 2.5-fold of MPI 1 hour post injection of the photoacoustic contrast agent [14].

Fluorescence images were acquired every 15 min after the administration of the nanoparticles. Intense fluorescence was observed in the $AlCl_3$ treated area of the targeted group, with intensity gradually increasing post injection and peaking at 15 min post injection (Fig. 6C). The average radiant efficiency (ARE) of the fluorescence increased from 5 min to 15 min post injection and remain stable until 60 min (6F). Our findings, are similar with results of FI with IR780 dye that was reported by Jung et al. [71]. The FI signal was significantly high with fluorescence intensity generated from IR780 dye observed from 5 min and maintained strong signal intensity until 30 min. These findings demonstrated the potential use of AuIONP$^{(+)}$ in providing a more specific and sensitive method to detect thrombus, by facilitating multi-modality imaging.

3.6. *In vivo thrombolysis*

Encouraged by the positive results from the diagnostic imaging, we further investigated the potential of AuIONP$^{(+)}$ as a thrombolysis therapy. The in vivo thrombosis model was conducted by exposing obstructed carotid arteries to 808 nm laser using the optimised setting obtained from the in vitro analysis. To evaluate the extent of the successful thrombolysis occurring after laser treatment, a change in blood flow was observed with a 0.5 mm flow probe which was recorded before and after the laser treatment. As seen in Fig. 7A, a significant change between the maximum and minimum value of flow recorded by the flow

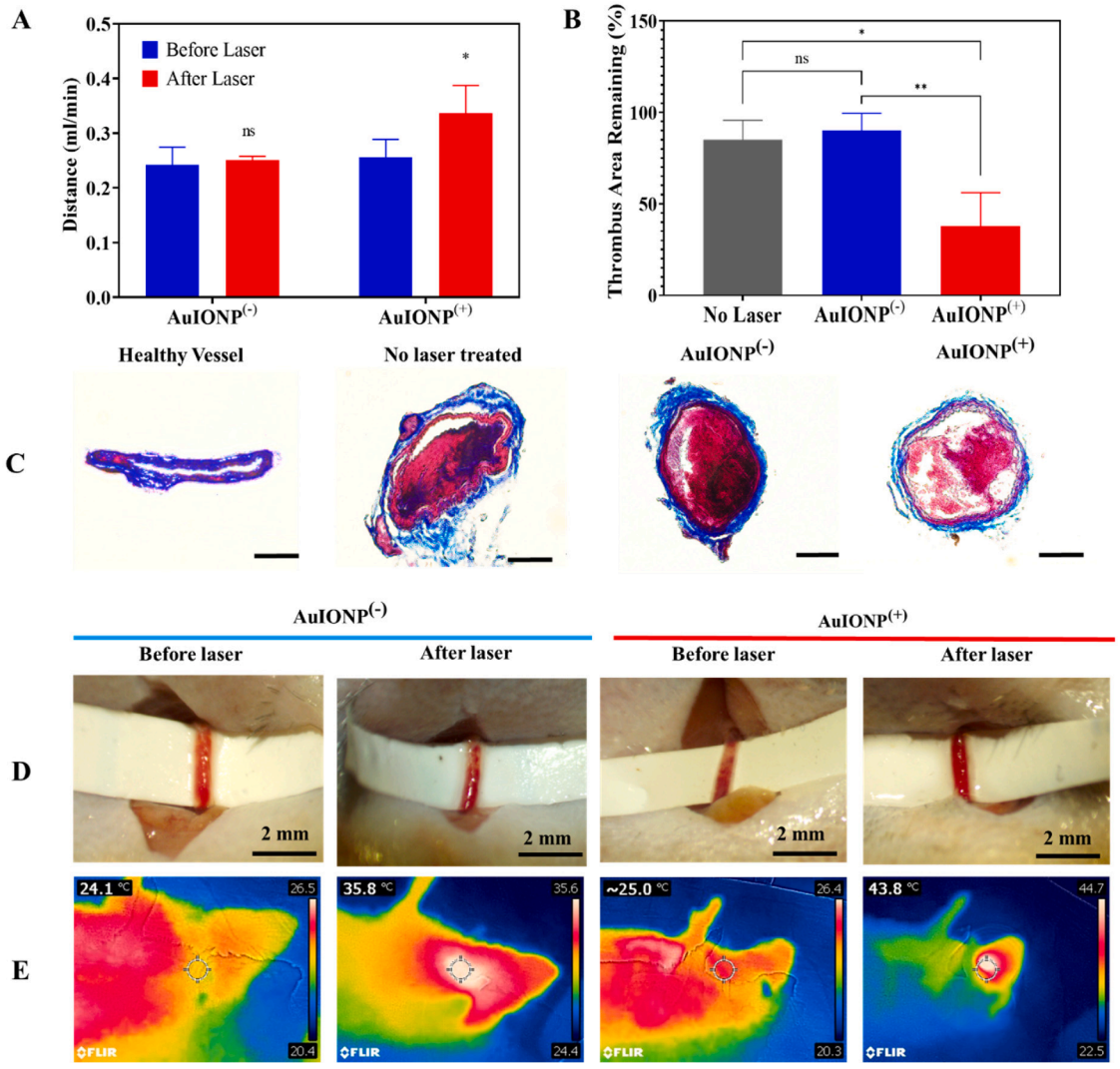

Fig. 7. In vivo photothermal thrombolysis sensitised by AuIONP. (A) Graph representing the difference between maximum and minimum value (distance) of flow reading, AuIONP$^{(+)}$ treated groups exhibiting higher change in flow after laser. (B) Thrombus area remaining between the non-targeted and targeted group indicating a significant reduction of the thrombus area in the laser treated targeted group ($n = 4$; ns $p > 0.05$, * $P < 0.05$, ** $P < 0.01$). (C) Histology of sectioned carotid arteries, thrombus area appeared as red after staining with Masson's trichrome (scale bar = 100 μm). (D) Documented images of the thrombus before and after exposure of laser in AuIONP$^{(-)}$ (blue line) and scFv-AuIONP (red line). Thrombus was still apparent in the AuIONP$^{(-)}$ group. (E) Infrared thermal images of AuIONP$^{(+)}$ (red line), exhibiting a higher temperature than AuIONP$^{(-)}$ (blue line).

probe was observed in the AuIONP$^{(+)}$ group. Figure S8 showed the changes in blood flow before and after laser treatment. Conversely, no significant changes of flow were exhibited by the non-targeted group. These findings, despite promising, needed further confirmation.

In order to further quantify the obtained results from flow observation, a histology examination was conducted on the sectioned carotid arteries. After Masson's Trichrome staining, a contrast difference between the blood vessel (blue) and wall adherent thrombus (bright red) was visible (Fig. 7C). The $AlCl_3$ treatment was able to produce a strong stable thrombus inside the vessel, as observed from the thrombus seen in the no laser-treated group. From the histology assessments, AuIONP$^{(-)}$ group showed significantly larger thrombus area remaining after laser treatment, possibly due to the low binding and targeting ability, leading to insufficient localised hyperthermia to lyse the thrombus (Fig. 7B). Promisingly, the AuIONP$^{(+)}$, demonstrated a smaller thrombus area, indicating the ability of laser treatment to facilitate thrombolysis.

Furthermore, a change visually was notable, with the AuIONP$^{(+)}$ group displaying less prominent thrombus inside the vessel after laser when compared to the AuIONP$^{(-)}$ (Fig. 7D). Additionally, a higher change in temperature for the AuIONP$^{(+)}$ was recorded by the infrared thermal camera, with the AuIONP$^{(+)}$ recording a temperature increase of ~19.5 °C, while compared to the modest increase of ~10.7 °C for the AuIONP$^{(-)}$ (Fig. 7E). This observation signifies the accumulation of AuIONP on the thrombus allowed for a more prominent increase in temperature. Furthermore, the temperature that was generated during in vivo thrombolysis with the AuIONP$^{(+)}$ was well maintained within 40–46 °C (Figure S9). Compared to previous research, our AuIONP$^{(+)}$ system application was not limited to only molecular imaging for thrombosis but could significantly facilitate thrombolysis without combination with pharmacological thrombolytics. Most of the development for theranostics incorporate thrombolytics, which have been proven effective but not without potential severe fatal side effects such as bleeding [72]. From the results we have obtained, the residual thrombus area of the AuIONP$^{(+)}$ group was significantly lower than AuIONP$^{(-)}$ and no laser group, with only around 50% of thrombus area remaining. AuIONP$^{(+)}$ performed better than other reported photothermal nanoparticles, such as the polydoamine mesoporous silica system which was developed by Zhong *et al.*, which demonstrate thrombus area remaining of around 70% after 10 min exposure to 1.0 W of NIR II laser [73]. Furthermore, our findings also indicate that AuIONP$^{(+)}$ has similar potential in reducing thrombus, to an intravenous injection of urokinase [38,73].

3.7. Biocompatibility of AuIONP

In order to ensure the AuIONP is suitable for biomedical applications, compatibility with macrophage cells were analysed with PrestoBlue method. The ability of active cells to metabolically reduce the reagent and produce colorimetric changes was used as an indicator to quantify the viability of cells in culture. No signs of cell toxicity were observed at a concentration of 200 ppm (Figure S10). The compatibility and effect of laser treatment (808 nm, 1.5 W/cm^2) were further analysed in smooth vascular endothelial cells (SVEC), exposed with the same intensity and time as the optimised protocol for in vivo. Endothelial cells after laser exposure remained 80% viability, with no significant difference in viability between the PBS and AuIONP treated cells, indicated by the bright fluorescence of the live cells stained by calcein AM (Figure S11). When applying the laser (808 nm, 1.5 W/cm^2) on mouse carotid arteries for thrombolysis, no damage to the blood vessels and surrounding tissues was observed. This finding is corroborated by previous reports which utilised stronger laser intensity (> 1.5 W/cm^2) and longer continuous exposure time with no adverse effect. In their studies, Zhang et al. and Zhao et al. applied NIR laser with a 2 W/cm^2 intensity for 20 and 15 min respectively, with no significant changes on the organs or healthy tissue surrounding the artery [14,74]. Additionally, Avila-Gomez et al. reported that mild hyperthermia had shown significant benefit towards improvement of reperfusion after thrombosis [75]. A temperature is considered mild hyperthermia or low temperature photothermal therapy when the exposed area temperature is between 43 and 45 °C, which is within the temperature range that our AuIONP generated after laser exposure in vivo [76]. Furthermore, blood compatibility was analysed with the observation of haemolysis percentage by incubating washed red blood cells in samples and the percentage was calculated by comparison with totally lysed sample (Triton-X 100) and negative control, which produced no lysis (PBS). As shown in Figure S12, PEGSH-AuIONP had minimal effect on the red blood cell lysis. Haemolysis percentage below 2% is considered non-haemolytic, indicating that particles with the concentrations tested did not induce haemolysis [77,78].

To ascertain the biocompatibility of AuIONP in organs, we collected vital organs from the treated mice, observed the distribution based on ex vivo fluorescence and microscopically observed the morphology of the sectioned tissues. From the images collected, there was no abnormality detected in those vital organs when compared to the non-treated mice, further emphasising the biocompatibility of the AuIONP administered (Figure S13). Based on the ex vivo radiant efficiency results, we tracked the accumulation of AuIONP$^{(+)}$ and AuIONP$^{(-)}$ in the vital organs. There is no prior study observing the biodistribution of AuIONP, however when comparing to gold and iron oxide NP biodistribution we obtained similar results [79]. AuIONPs were accumulated mostly in the liver and kidney, with no significant difference of radiant efficiency between AuIONP$^{(+)}$ and AuIONP$^{(-)}$ treated groups (Figure S14) [80,81].

Conclusion

In summary, we have demonstrated the ability of AuIONP$^{(+)}$ as a theranostic agent for thrombosis with efficient targeting towards activated platelets and triple modality imaging. With the enhanced targeting, AuIONP$^{(+)}$ was able to specifically bind and emit stronger MRI contrast and photoacoustic signal on the location of the thrombus. Furthermore, through NIR laser photothermal trigger and biocompatibility studies, AuIONP$^{(+)}$ enhanced thrombolysis and was highly compatible. Although complete elimination of thrombus was not observed in this study, a partial restoration of blood flow and opening of the blood vessel lumen was achieved, which would be highly beneficial for emergency treatment of thrombosis-related events. Overall, this study provides additional perspective on the utilisation of theranostic nanoparticles for MRI, PAI and FLI, as well as therapeutic applications for rapid thrombolysis.

CRediT authorship contribution statement

Najma Annuria Fithri: Investigation, Formal analysis, Writing – original draft, Visualization. **Yuao Wu:** Investigation, Formal analysis. **Gary Cowin:** Investigation, Formal analysis. **Fahima Akhter:** Investigation, Formal analysis. **Huong D.N. Tran:** Investigation, Validation, Formal analysis. **Brian Tse:** Investigation, Formal analysis. **Nicholas Westra van Holthe:** Investigation, Formal analysis. **Shehzahdi S. Moonshi:** Investigation, Formal analysis. **Karlheinz Peter:** Supervision, Resources, Writing – review & editing. **Xiaowei Wang:** Supervision, Resources, Writing – review & editing. **Nghia P. Truong:** Supervision, Resources, Funding acquisition, Writing – review & editing. **Hang Thu Ta:** Conceptualization, Methodology, Supervision, Resources, Writing – review & editing, Project administration, Funding acquisition.

Declaration of Competing Interest

The authors declare the following financial interests/personal relationships which may be considered as potential competing interests:

Hang Thu Ta reports financial support was provided by National Health and Medical Research Council. Hang Thu Ta reports financial support was provided by National Heart Foundation of Australia. Nghia

Truong PHuoc reports financial support was provided by Australian Research Council.

Data availability

Data will be made available on request.

Acknowledgment

N.A.F. acknowledges the financial support in the form of PhD scholarship funded by Australia Awards Program. H.T.T and N.P.T. acknowledge the funding support of an Ideas grant (APP2002827) from the National Health and Medical Research Council. H.T.T is supported by a Heart Foundation Future Leader Fellowship (102761) and NHMRC grants (APP1037310, APP1182347). N.P.T. is grateful for the award of a DECRA Fellowship (DE180100076) and a Discovery Project grant (DP200100231) from the Australian Research Council. K.P is supported by an NHMRC Investigator Fellowship. X.W is supported by a National Heart Foundation Future Leader Fellowship and a Baker Fellowship.

Supplementary materials

Supplementary material associated with this article can be found, in the online version, at doi:10.1016/j.apmt.2023.101750.

References

[1] A.M. Wendelboe, G.E. Raskob, Global burden of thrombosis: epidemiologic aspects, Circ. Res. 118 (9) (2016) 1340–1347.
[2] R. Oklu, Thrombosis, Cardiovasc Diagn Ther 7 (2017) S131–S133.
[3] K. Satoh, T. Satoh, N. Yaoita, H. Shimokawa, Recent Advances in the understanding of thrombosis, Arterioscler. Thromb. Vasc. Biol. 39 (6) (2019) e159–e165.
[4] L. Ortega-Paz, D. Capodanno, G. Montalescot, D.J. Angiolillo, Coronavirus disease 2019-associated thrombosis and coagulopathy: review of the pathophysiological characteristics and implications for antithrombotic management, J. Am. Heart Assoc. 10 (3) (2021), e019650.
[5] P.R. Hunter, Thrombosis after covid-19 vaccination, BMJ 373 (2021) n958.
[6] P. Russel, C.E. Hagemeyer, L. Esser, N.H. Voelcker, Theranostic nanoparticles for the management of thrombosis, Theranostics 12 (6) (2022) 2773–2800.
[7] O. Angeras, I. Haraldsson, B. Redfors, O. Frobert, P. Petursson, P. Albertsson, D. Ioanes, J. Odenstedt, H. Olsson, N. Witt, A. Ruck, J. Millgard, J. Nilsson, J. Persson, M. Soderbom, H. Wedel, D. Erlinge, S. James, T. Ramunddal, E. Omerovic, Impact of thrombus aspiration on mortality, stent thrombosis, and stroke in patients with ST-segment-elevation myocardial infarction: a report from the swedish coronary angiography and angioplasty registry, J. Am. Heart Assoc. 7 (1) (2018).
[8] K.P. Rentrop, F. Feit, Reperfusion therapy for acute myocardial infarction: concepts and controversies from inception to acceptance, Am. Heart J. 170 (5) (2015) 971–980.
[9] Q. Pan, J. Xu, C.J. Wen, Y.Y. Xiong, Z.T. Gong, Y.J. Yang, Nanoparticles: promising tools for the treatment and prevention of myocardial infarction, Int. J. Nanomed. 16 (2021) 6719–6747.
[10] H.T. Ta, N. Arndt, Y. Wu, H.J. Lim, S. Landeen, R. Zhang, D. Kamato, P.J. Little, A. K. Whittaker, Z.P. Xu, Activatable magnetic resonance nanosensor as a potential imaging agent for detecting and discriminating thrombosis, Nanoscale 10 (31) (2018) 15103–15115.
[11] D. Collen, H.R. Lijnen, Thrombolytic agents, Thromb. Haemost. 93 (4) (2005) 627–630.
[12] N. Singh, A. Varma, A. Verma, B.N. Maurya, D. Dash, Relief from vascular occlusion using photothermal ablation of thrombus with a multimodal perspective, Nano Res. 9 (8) (2016) 2327–2337.
[13] Z. Qin, J.C. Bischof, Thermophysical and biological responses of gold nanoparticle laser heating, Chem. Soc. Rev. 41 (3) (2012) 1191–1217.
[14] F. Zhang, Y. Liu, J. Lei, S. Wang, X. Ji, H. Liu, Q. Yang, Metal-organic-framework-derived carbon nanostructures for site-specific dual-modality photothermal/photodynamic thrombus therapy, Adv Sci (Weinh) 6 (17) (2019), 1901378.
[15] J. Beik, M. Asadi, S. Khoei, S. Laurent, Z. Abed, M. Mirrahimi, A. Farashahi, R. Hashemian, H. Ghaznavi, A. Shakeri-Zadeh, Simulation-guided photothermal therapy using MRI-traceable iron oxide-gold nanoparticle, J. Photochem. Photobiol. B 199 (2019), 111599.
[16] M. Varna, H.V. Xuan, E. Fort, Gold nanoparticles in cardiovascular imaging, Wiley Interdisciplinary, Rev. Nanomed. Nanobiotechnol. 10 (1) (2018).
[17] I. Cicha, Thrombosis: novel nanomedical concepts of diagnosis and treatment, World J. Cardiol. 7 (8) (2015) 434–441.
[18] G.Y. Karande, S.S. Hedgire, Y. Sanchez, V. Baliyan, V. Mishra, S. Ganguli, A. M. Prabhakar, Advanced imaging in acute and chronic deep vein thrombosis, Cardiovasc. Diagn. Ther. 6 (6) (2016) 493–507.
[19] G.G. Gasparian, N. Sanossian, M.S. Shiroishi, D.S. Liebeskind, Imaging of occlusive thrombi in acute ischemic stroke, Int. J. Stroke 10 (3) (2015) 298–305.
[20] P. Rajiah, M.Y. Desai, D. Kwon, S.D. Flamm, MR imaging of myocardial infarction, Radiographics (2013) 33.
[21] C. Detter, S. Wipper, D. Russ, A. Iffland, L. Burdorf, E. Thein, K. Wegscheider, H. Reichenspurner, B. Reichart, Fluorescent cardiac imaging: a novel intraoperative method for quantitative assessment of myocardial perfusion during graded coronary artery stenosis, Circulation 116 (9) (2007) 1007–1014.
[22] J. Hu, D.H. Ortgies, E. Martín Rodríguez, F. Rivero, R. Aguilar Torres, F. Alfonso, N. Fernández, G. Carreño-Tarragona, L. Monge, F. Sanz-Rodriguez, M.d.C. Iglesias, M. Granado, A.L. García-Villalon, J. García Solé, D. Jaque, Optical nanoparticles for cardiovascular imaging, Adv. Opt. Mater. 6 (22) (2018).
[23] M. Varna, H.V. Xuan, E. Fort, Gold nanoparticles in cardiovascular imaging, Wiley Interdiscip. Rev. Nanomed. Nanobiotechnol. 10 (1) (2018).
[24] K. Jansen, M. Wu, A.F. van der Steen, G. van Soest, Photoacoustic imaging of human coronary atherosclerosis in two spectral bands, Photoacoustics 2 (1) (2014) 12–20.
[25] H. Zafar, M. Leahy, W. Wijns, M. Kolios, J. Zafar, N. Johnson, F. Sharif, Photoacoustic cardiovascular imaging: a new technique for imaging of atherosclerosis and vulnerable plaque detection, Biomed. Phys. Eng. Express 4 (3) (2018).
[26] N.N.M. Yusof, A. McCann, P.J. Little, H.T.J.T.r. Ta, Non-invasive imaging techniques for the differentiation of acute and chronic thrombosis, Thromb. Res. 177 (2019) 161–171.
[27] K.X. Vazquez-Prada, J. Lam, D. Kamato, Z.P. Xu, P.J. Little, H.T.J.A. Ta, Thrombosis, V. Biology, Targeted molecular imaging of cardiovascular diseases by iron oxide nanoparticles, Arterioscler. Thromb. Vasc. Biol. 41 (2) (2021) 601–613.
[28] Y. Liu, Y. Wu, R. Zhang, J. Lam, J.C. Ng, Z.P. Xu, L. Li, H.T.J.A.A.B.M. Ta, Investigating the use of layered double hydroxide nanoparticles as carriers of metal oxides for theranostics of ROS-related diseases, ACS Appl. Bio Mater. 2 (12) (2019) 5930–5940.
[29] Y. Wu, R. Zhang, H.D. Tran, N.D. Kurniawan, S.S. Moonshi, A.K. Whittaker, H.T.J. A.A.N.M. Ta, Chitosan nanococktails containing both ceria and superparamagnetic iron oxide nanoparticles for reactive oxygen species-related theranostics, ACS Appl. Nano Mater. 4 (4) (2021) 3604–3618.
[30] N. Arndt, H.D. Tran, R. Zhang, Z.P. Xu, H.T.J.A.S. Ta, Different approaches to develop nanosensors for diagnosis of diseases, Adv. Sci. 7 (24) (2020), 2001476.
[31] Y. Wu, K.X. Vazquez-Prada, Y. Liu, A.K. Whittaker, R. Zhang, H.T.J.N. Ta, Recent advances in the development of theranostic nanoparticles for cardiovascular diseases, Nanotheranostics 5 (4) (2021) 499.
[32] A.U. Rehman, Y. Wu, H.D. Tran, K. Vazquez-Prada, Y. Liu, H. Adelnia, N. D. Kurniawan, M.N. Anjum, S.S. Moonshi, H.T.J.A.A.N.M. Ta, Silver/iron oxide nano-popcorns for imaging and therapy, ACS Appl. Nano Mater. 4 (10) (2021) 10136–10147.
[33] Y. Wu, G. Cowin, S.S. Moonshi, H.D. Tran, N.A. Fithri, A.K. Whittaker, R. Zhang, H. T.J.M.S. Ta, E. C, Engineering chitosan nano-cocktail containing iron oxide and ceria: a two-in-one approach for treatment of inflammatory diseases and tracking of material delivery, Mater. Sci. Eng. C 131 (2021), 112477.
[34] S.S. Moonshi, Y. Wu, H.T.J.W.I.R.N. Ta, Nanobiotechnology, Visualizing stem cells in vivo using magnetic resonance imaging, WIRES Nanomed. Nanobiotechnol. 14 (2) (2022) e1760.
[35] X. Wang, Y. Gkanatsas, J. Palasubramaniam, J.D. Hohmann, Y.C. Chen, B. Lim, C. E. Hagemeyer, K. Peter, Thrombus-targeted theranostic microbubbles: a new technology towards concurrent rapid ultrasound diagnosis and bleeding-free fibrinolytic treatment of thrombosis, Theranostics 6 (5) (2016) 726–738.
[36] D. Hanjaya-Putra, C. Haller, X. Wang, E. Dai, B. Lim, L. Liu, P. Jaminet, J. Yao, A. Searle, T. Bonnard, C.E. Hagemeyer, K. Peter, E.L. Chaikof, Platelet-targeted dual pathway antithrombotic inhibits thrombosis with preserved hemostasis, JCI Insight 3 (15) (2018).
[37] A. Zia, Y. Wu, T. Nguyen, X. Wang, K. Peter, H.T.J.C.r. Ta, The choice of targets and ligands for site-specific delivery of nanomedicine to atherosclerosis, Cardiovasc. Res. 116 (13) (2020) 2055–2068.
[38] X. Wang, C.E. Hagemeyer, J.D. Hohmann, E. Leitner, P.C. Armstrong, F. Jia, M. Olschewski, A. Needles, K. Peter, I. Ahrens, Novel single-chain antibody-targeted microbubbles for molecular ultrasound imaging of thrombosis: validation of a unique noninvasive method for rapid and sensitive detection of thrombi and monitoring of success or failure of thrombolysis in mice, Circulation 125 (25) (2012) 3117–3126.
[39] L.L. Ma, M.D. Feldman, J.M. Tam, A.S. Paranjape, K.K. Cheruku, T.A. Larson, J. O. Tam, D.R. Ingram, V. Paramita, J.W. Villard, J.T. Jenkins, T. Wang, G.D. Clarke, R. Asmis, K. Sekolov, B. Chandrasekar, T.E. Milner, K.P. Johnston, Small multifunctional nanoclusters (nanoroses) for targeted cellular imaging and therapy, ACS Nano 3 (2009) 2686–2696.
[40] H.T. Ta, Z. Li, C.E. Hagemeyer, G. Cowin, S. Zhang, J. Palasubramaniam, K. Alt, X. Wang, K. Peter, A.K. Whittaker, Molecular imaging of activated platelets via antibody-targeted ultra-small iron oxide nanoparticles displaying unique dual MRI contrast, Biomaterials 134 (2017) 31–42.
[41] H.S. Oh, Novel Theranostic Material for Thrombosis, University of Queensland, 2019.
[42] Y. Gossuin, S. Disch, Q.L. Vuong, P. Gillis, R.P. Hermann, J.H. Park, M.J. Sailor, NMR relaxation and magnetic properties of superparamagnetic nanoworms, Contrast Media Mol. Imaging 5 (6) (2010) 318–322.

[43] C. Hoskins, Y. Min, M. Gueorguieva, C. McDougall, A. Volovick, P. Prentice, Z. Wang, A. Melzer, A. Cuschieri, L. Wang, Hybrid gold-iron oxide nanoparticles as a multifunctional platform for biomedical application, J. Nanobiotechnol. 10 (2012) 1–12.
[44] J.-.W. Park, J.S. Shumaker-Perry, Strong resistance of citrate anions on metal nanoparticles to desorption under thiol functionalization, ACS Nano 9 (2) (2015) 1665–1682.
[45] T. Honold, D. Skrybeck, K.G. Wagner, M. Karg, Fully reversible quantitative phase transfer of gold nanoparticles using bifunctional PNIPAM ligands, Langmuir 33 (1) (2017) 253–261.
[46] E. Pensa, E. Cortes, G. Corthey, P. Carro, C. Vericat, M.H. Fonticelli, G. Benitez, A. A. Rubert, R.C. Salvarezza, The chemistry of the sulfur-gold interface: in search of a unified model, Acc. Chem. Res. 45 (8) (2012) 1183–1192.
[47] I. Antal, O. Strbak, I. Khmara, M. Koneracka, M. Kubovcikova, V. Zavisova, M. Kmetova, E. Baranovicova, D. Dobrota, MRI relaxivity changes of the magnetic nanoparticles induced by different amino acid coatings, Nanomaterials (Basel) 10 (2) (2020).
[48] G. Brennan, S. Bergamino, M. Pescio, S.A.M. Tofail, C. Silien, The effects of a varied gold shell thickness on iron oxide nanoparticle cores in magnetic manipulation, T1 and T2 MRI contrasting, and magnetic hyperthermia, Nanomaterials (Basel) 10 (12) (2020).
[49] S. Sourbron, M. Heilmann, C. Walczak, J. Vautier, L.R. Schad, A. Volk, T2*-relaxivity contrast imaging: first results, Magn. Reson. Med. 69 (5) (2013) 1430–1437.
[50] R. García-Álvarez, L. Chen, A. Nedilko, A. Sánchez-Iglesias, A. Rix, W. Lederle, V. Pathak, T. Lammers, G. von Plessen, K. Kostarelos, L.M. Liz-Marzán, A.J. C. Kuehne, D.N. Chigrin, Optimizing the geometry of photoacoustically active gold nanoparticles for biomedical imaging, ACS Photonics 7 (3) (2020) 646–652.
[51] W. Li, X. Chen, Gold nanoparticles for photoacoustic imaging, Nanomedicine 10 (2) (2015) 299–320.
[52] S. Wang, J. Lin, T. Wang, X. Chen, P. Huang, Recent advances in photoacoustic imaging for deep-tissue biomedical applications, Theranostics 6 (13) (2016) 2394–2413.
[53] L. Li, L.V. Wang, Recent advances in photoacoustic tomography, BME Front. 2021 (2021) 1–17.
[54] J.P.F. Werner, Y. Huang, K. Mishra, R. Janowski, P. Vetschera, A. Chmyrov, D. Niessing, V. Ntziachristos, A.C. Stiel, Challenging a preconception: optoacoustic spectrum differs from the absorption spectrum of proteins and dyes for molecular imagin, Anal. Chem. (2020).
[55] Q. Fan, K. Cheng, Z. Yang, R. Zhang, M. Yang, X. Hu, X. Ma, L. Bu, X. Lu, X. Xiong, W. Huang, H. Zhao, Z. Cheng, Perylene-diimide-based nanoparticles as highly efficient photoacoustic agents for deep brain tumor imaging in living mice, Adv. Mater. 27 (5) (2015) 843–847.
[56] X. Wang, J. Palasubramaniam, Y. Gkanatsas, J.D. Hohmann, E. Westein, R. Kanojia, K. Alt, D. Huang, F. Jia, I. Ahrens, R.L. Medcalf, K. Peter, C. E. Hagemeyer, Towards effective and safe thrombolysis and thromboprophylaxis: preclinical testing of a novel antibody-targeted recombinant plasminogen activator directed against activated platelets, Circ. Res. 114 (7) (2014) 1083–1093.
[57] H.T. Ta, S. Prabhu, E. Leitner, F. Jia, D. von Elverfeldt, K.E. Jackson, T. Heidt, A. K. Nair, H. Pearce, C. von Zur Muhlen, X. Wang, K. Peter, C.E. Hagemeyer, Enzymatic single-chain antibody tagging: a universal approach to targeted molecular imaging and cell homing in cardiovascular disease, Circ. Res. 109 (4) (2011) 365–373.
[58] S. Li, T. Zhang, Z. Zhu, N. Gao, Q.-.H. Xu, Lighting up the gold nanoparticles quenched fluorescence by silver nanoparticles: a separation distance study, RSC Adv. 6 (63) (2016) 58566–58572.
[59] M.V.A. van Moorsel, R.T. Urbanus, S. Verhoef, C.A. Koekman, M. Vink, T. Vermonden, C. Maas, G. Pasterkamp, R.M. Schiffelers, A head-to-head comparison of conjugation methods for VHHs: random maleimide-thiol coupling versus controlled click chemistry, Int. J. Pharm. X 1 (2019), 100020.
[60] N.K. Lee, C.J. Wang, J. Lim, W. Park, H.K. Kwon, S.N. Kim, T.H. Kim, C.G. Park, Impact of the conjugation of antibodies to the surfaces of polymer nanoparticles on the immune cell targeting abilities, Nano Converg. 8 (1) (2021) 24.
[61] F. Akther, J. Zhang, H.D.N. Tran, H. Fallahi, H. Adelnia, H.P. Phan, N.T. Nguyen, H.T. Ta, Atherothrombosis-on-chip: a site-specific microfluidic model for thrombus formation and drug discovery, Adv. Biol. (Weinh) 6 (7) (2022), e2101316.
[62] H.T. Ta, N.P. Truong, A.K. Whittaker, T.P. Davis, K. Peter, The effects of particle size, shape, density and flow characteristics on particle margination to vascular walls in cardiovascular diseases, Expert Opin. Drug Deliv. 15 (1) (2018) 33–45.
[63] A. Guo, Y. Fu, G. Wang, X. Wang, Diameter effect of gold nanoparticles on photothermal conversion for solar steam generation, RSC Adv. 7 (8) (2017) 4815–4824.
[64] Y. Liu, J. Kangas, Y. Wang, K. Khosla, J. Pasek-Allen, A. Saunders, S. Oldenburg, J. Bischof, Photothermal conversion of gold nanoparticles for uniform pulsed laser warming of vitrified biomaterials, Nanoscale 12 (23) (2020) 12346–12356.
[65] Q. Tian, F. Jiang, R. Zou, Q. Liu, Z. Chen, M. Zhu, S. Yang, J. Wang, J. Wang, J. Hu, Hydrophilic Cu_9S_5: a photothermal agent with a 25.7% conversion efficiency for photothermal ablation of cancer cells in vivo, ACS Nano 5 (2011) 9761–9771.
[66] H. Chen, L. Shao, T. Ming, Z. Sun, C. Zhao, B. Yang, J. Wang, Understanding the photothermal conversion efficiency of gold nanocrystals, Small 6 (20) (2010) 2272–2280.
[67] Z. Qin, Y. Wang, J. Randrianalisoa, V. Raeesi, W.C. Chan, W. Lipinski, J.C. Bischof, Quantitative comparison of photothermal heat generation between gold nanospheres and nanorods, Sci. Rep. 6 (2016) 29836.
[68] A. Lawrie, S. Kitchen, G. Purdy, I. Mackie, F. Preston, S. Machin, Assessment of Actin FS and Actin FSL sensitivity to specific clotting factor deficiencies, Clin. Lab. Haem. 20 (1998) 179–186.
[69] T. Bonnard, C.E. Hagemeyer, Ferric chloride-induced thrombosis mouse model on carotid artery and mesentery vessel, J. Vis. Exp. (100) (2015) e52838.
[70] M. Wolters, R.H. van Hoof, A. Wagenaar, K. Douma, M.A. van Zandvoort, T. H. Hackeng, M.J. Post, W.H. Backes, M.E. Kooi, MRI artifacts in the ferric chloride thrombus animal model: an alternative solution: preventing MRI artifacts after thrombus induction with a non-ferromagnetic Lewis acid, J. Thromb. Haemost. 11 (9) (2013) 1766–1769.
[71] E. Jung, C. Kang, J. Lee, D. Yoo, D.W. Hwang, D. Kim, S.C. Park, S.K. Lim, C. Song, D. Lee, Molecularly engineered theranostic nanoparticles for thrombosed vessels: H2O2-activatable contrast-enhanced photoacoustic imaging and antithrombotic therapy, ACS Nano 12 (1) (2018) 392–401.
[72] L.M. Brass, J.H. Lichtman, Y. Wang, J.H. Gurwitz, M.J. Radford, H.M. Krumholz, Intracranial hemorrhage associated with thrombolytic therapy for elderly patients with acute myocardial infarction, Stroke 31 (8) (2000) 1802–1811.
[73] Z. Zhong, C. Fang, S. He, T. Zhang, S. Liu, Y. Zhang, Q. Wang, X. Ding, W. Zhou, X. Wang, Sequential release platform of heparin and urokinase with dual physical (NIR-II and bubbles) assistance for deep venous thrombosis, ACS Biomater. Sci. Eng. 6 (12) (2020) 6790–6799.
[74] Z. Zhao, X. Zhang, H. Zhang, X. Shan, M. Bai, Z. Wang, F. Yang, H. Zhang, Q. Kan, B. Sun, J. Sun, Z. He, C. Luo, Elaborately engineering a self-indicating dual-drug nanoassembly for site-specific photothermal-potentiated thrombus penetration and thrombolysis, Adv. Sci. (Weinh) 9 (4) (2022), e2104264.
[75] P. Avila-Gomez, P. Hervella, A. Da Silva-Candal, M. Perez-Mato, M. Rodriguez-Yanez, I. Lopez-Dequidt, J.M. Pumar, J. Castillo, T. Sobrino, R. Iglesias-Rey, F. Campos, Temperature-induced changes in reperfused stroke: inflammatory and thrombolytic biomarkers, J. Clin. Med. 9 (7) (2020).
[76] X. Deng, Z. Shao, Y. Zhao, Solutions to the drawbacks of photothermal and photodynamic cancer therapy, Adv. Sci. (Weinh) 8 (3) (2021), 2002504.
[77] A. Mesdaghinia, Z. Pourpak, K. Naddafi, R.N. Nodehi, Z. Alizadeh, S. Rezaei, A. Mohammadi, M. Faraji, An in vitro method to evaluate hemolysis of human red blood cells (RBCs) treated by airborne particulate matter (PM10), MethodsX 6 (2019) 156–161.
[78] J. Reguera, D. Jimenez de Aberasturi, M. Henriksen-Lacey, J. Langer, A. Espinosa, B. Szczupak, C. Wilhelm, L.M. Liz-Marzan, Janus plasmonic-magnetic gold-iron oxide nanoparticles as contrast agents for multimodal imaging, Nanoscale 9 (27) (2017) 9467–9480.
[79] M.A.M. Tarkistani, V. Komalla, V. Kayser, Recent advances in the use of iron-gold hybrid nanoparticles for biomedical applications, Nanomaterials (Basel) 11 (5) (2021).
[80] J.J. Hue, H.J. Lee, S. Jon, S.Y. Nam, Y.W. Yun, J.S. Kim, B.J. Lee, Distribution and accumulation of Cy5.5-labeled thermally cross-linked superparamagnetic iron oxide nanoparticles in the tissues of ICR mice, J. Vet. Sci. 14 (4) (2013) 473–479.
[81] S.K. Balasubramanian, J. Jittiwat, J. Manikandan, C.N. Ong, L.E. Yu, W.Y. Ong, Biodistribution of gold nanoparticles and gene expression changes in the liver and spleen after intravenous administration in rats, Biomaterials 31 (8) (2010) 2034–2042.

Supplementary Materials:

Gold-Iron Oxide Nanoparticle: A Unique Multimodal Theranostic Approach for Thrombosis

Materials

Hydrochloroauric acid (Sigma), trisodium citrate (Fisher Scientific), hydroxylamine 50% (SigmaAldrich), sodium hydroxide pellet (SigmaAldrich), COOH-PEGSH (7500 g/mol) and mPEGSH (6000 g/mol) (SigmaAldrich), MES hydrate (SigmaAldrich), Cy5 (Lumiprobe), EDC (1-ethyl-3-(3-dimethylaminopropyl)carbodiimide hydrochloride) (ThermoFisher Scientific), $DiOC_6$ (3,3'-dihexyloxacarbocyanine Iodide) dye (SigmaAldrich), phosphate buffer saline tablet (SigmaAldrich), single chain antibody (scFv SCE-5 LPETG) and sortase A enzyme was produced by a team in Baker Institute, Gly-CONH-PEG_3-N_3 (Click Chemistry Tools), dibenzoazacyclooctyne (DBCO) (Click Chemistry Tools), purifying resin (TALON®), micro bichinchoninic (BCA) protein assay kit (Thermo Scientific), ammonium persulfate (Bio-rad), TEMED (Bio-rad), acrylamide/bis (Bio-rad), Trizma base (SigmaAldrich), tris-HCl (SigmaAldrich), Coomassie blue stain (Bio-rad), stained molecular weight marker (Precision Plus-Bio-rad), Triton-X 100 (SigmaAldrich), Actin FSL (Dade Siemens), calcium chloride dihydrate (SigmaAldrich), low EEO agarose (Sigma), agarose low gelling (SigmaAldrich), ethylendiaminetetracetic acid (Sigma), isopropanol (Merck), nitric acid (Merck), glacial acetic acid (Merck), PrestoBlue (Invitrogen), and Calcein AM (Invitrogen).

Synthesis and characterisation of PEGSH-AuIONP

Gold coated iron oxide (AuIONP) was prepared using a seeding method which was modified from Ma *et al*. In a glass flask, 127 µL of 10.1 mM citrate-coated iron oxide (IONP) which was previously synthesised by previous protocol was added into a solution of double distilled water and let stir at 500 rpm. After 3 minutes, 7 µL of 50% hydroxylamine (Merck), 70 µL of 1.14% trisodium citrate (Merck), and and 75 µL of 0.1M sodium hydroxide (Merck) were introduced in succession to the solution. The mixture was then stirred for 3 minutes before adding 50 µL aliquot of 6.348 mM $HAuCl_4$ (Sigma). The solution was allowed to stir for 10 minutes before adding a further 50 µL of the HAuCl4, until a total of 200 µL aliquot of has been added. A gradual change in colour from yellowish orange to green/bluish brown was observed and a final 75 µL of trisodium citrate was added into the solution. Dense gold-coated iron oxide particles were obtained and separated from the uncoated IONP by centrifugation at 3500 g for 7 minutes. The sediment was then redispersed in water and the obtained combined

dispersion was dialysed using a 10k MWCO tube (Thermo Scientific) overnight. Coating with mPEGSH (MW: 6000 g/mol, Sigma) and COOH-PEGSH (MW: 7500 g/mol, Sigma-Aldrich) was established with a ligand exchange method. AuIONP was added dropwise into the polymer solution, with a polymer to AuIONP ratio of 5:1 based on mass. COOH-PEG-SH was added first into the mixture and allowed to stir for 1 hour. The particle was further attached with mPEG-SH (with a ratio mPEG-SH to COOH-PEG-SH of 2:1) by incubating the whole solution overnight before separation and washing by centrifugation at 1000 g for 6 minutes. Particle characterisation was performed using dynamic light scattering (DLS, Anton Paar Litesizer) and transmission electron microscopy (TEM, Hitachi 7700B). Prior to further in vitro and in vivo analysis, concentration of iron and gold were analysed using ICP-MS. Potential of T_2* and photoacoustic enhancing contrast agent PEGSH-AuIONP was determined by preparing phantoms from polystyrene tubes and analysed by the MRI 7T imaging system (Bruker) and multi spectra optoacoustic tomography (MSOT, inVision 256TF, iThera Medical) system in Centre of Advanced Imaging, The University of Queensland, Brisbane.

Conjugation of scFv-N_3 and Cy5 to PEGSH-AuIONP

A total of 1 mg PEGSH-AuIONP (containing 7.78 nmole COOH) was collected and dispersed in 0.1 M MES buffer pH 5 (Sigma). Into the solution 389 nmole EDC (Thermo Scientific) in DMSO (Merck) was added, vortexed and then sonicated for 10 minutes in a bath sonicator. The reaction was then maintained at 37 °C in a shaking incubator at 700 rpm for 20 minutes. DBCO (Click Chemistry Tools) and Cy5 (Lumiprobe) were added to the reaction with a molar ratio of 2:1 (3.88 and 1.94 nmole, respectively) and allowed to react for overnight. After overnight reaction, the particle was centrifuged at 1000 g and redispersed in MES buffer pH 6, with the washing process conducted twice to ensure elimination of unreacted components. With a mass ratio of 1:50 (scFv-N_3:DBCO-AuIONP) the antibody was added to the DBCO-AuIONP and the reaction was maintained at 37°C for overnight. Purification was conducted by washing the scFv-AuIONP with centrifugation at 1000 g for 3 times, and the resulting scFv-AuIONP dispersed in PBS 7.4 and stored in 4 °C until further use. In order to evaluate the conjugation efficiency, micro bicinchoninic (BCA) assay, sodium dodecyl sulphate-polyacrylamide gel electrophoresis (SDS-PAGE) and agarose gel electrophoresis was conducted with methodology explained in the supplementary material section.

Antibody to Azide Conjugation

The protocol that was utilised for this conjugation process was developed and modified from Ta et al . Prior to the reaction, sortase buffer was prepared by mixing 50 mM of Tris HCl,

150 mM of NaCl, and 0.5 mM of $CaCl_2$. Single chain antibody (scFv) SCE-5 was ligated to an azide containing peptide (NH2-Glycine-CONH-PEG_3-N_3) facilitated by sortase reaction. Peptide, sortase, and scFv were mixed in sortase buffer with a molar ratio of 3:1:1 for overnight at 37°C. Purification to remove unreacted his-tagged scFv and sortase were done by mixing with metal affinity resin (TALON®) for 20 minutes. The mixture was centrifuged and the supernatant was transferred to a 10k MWCO filter centrifugation unit to separate with unreacted peptide. The solution left on top of the filter is collected and analysed for characterisation by SDS Page and BCA assay. The resulting scFv-azide conjugate was stored in -20°C freezer.

SDS-Page

For scFv-azide analysis, SDS-page analysis with 12% acrylamide was performed. After the gel has been set, molecular weight marker, samples, and scFv standard was inserted into separate lanes. The gel was then run on 80 V until the samples formed a homogenous line at the end of stacking gel, then proceed to run at 120 V until good separation was established. Resulting gel was then incubated with Coomassie blue stain for 1 hour, and thoroughly destained. Imaging with Bio-rad XR+ was performed and the yield was then calculated based on the volume of signal intensity analysed on ImageLab software.

Bicinchoninic acid (BCA) – Assay

The assay was conducted using BCA protein assay reagent, by observing the colour intensity generated with a microplate reader. Five µL of sample was inserted into each well (replicate three times) and diluted 30x with the reagent. Incubate the sample at 37C for 2 hours and read the resulting absorbance at 562 nm. Bovine serum albumin (BSA) standard was used as the standard (range of 0 – 200 ppm) and yield was then calculated based on the BSA standard curve.

Agarose Gel Electrophoresis

Agarose gel 1% was prepared by dissolving agarose in tris acetate EDTA (TAE) buffer, by slowly heating the solution in low intensity microwave until the agarose was fully dissolved. The gel was then poured into the mold and comb was inserted to form homogenous wells. After the gel has set, 40 µl of samples that have been added with loading buffer (containing glycerol in TAE buffer) were carefully inserted into the wells. Separation was conducted by running the gel at 100V until satisfactory separation was achieved. The gel was then imaged with Bio-rad

XR+ under bright light mode.

AuIONP and SCE5-AuIONP Particle Characterisation

Size, polydispersity index and zeta potential were measured by dynamic light scattering method using Anton Paar Litesizer instrument with refractive index of iron oxide, water as a dispersant at 25°C. The absorption spectra of the resulting particles were scanned from 400-1000 nm using the absorbance mode in Clariostar plate reader (BMG Labtech) with 1 nm increment. Similarly, fluorescence intensity was measured using Clariostar plate reader with excitation of 610-620 nm and emission at 670-680 nm. The morphology and size of the resulting AuIONP was further analysed using a transmission electron microscope (TEM), with energy dispersive X-Ray spectroscopy (EDS) analysis to confirm the component. Stability of the AuIONP was tested by adding 180 µL of the sample and 20 µL of PBS 7.4 10x strength (volume ratio of 1:10) and mixed gently with a pipette. Absorbance reading at 808 nm was taken at 2, 4, 24 hour and 1 week after incubation. Percentage of absorbance decrease was calculated following Equation 1 below.

$$Percentage\ of\ absorption\ decrease\ (\%) = \frac{Absorbance\ at\ 24\ hour - Absorbance\ at\ 0\ hour}{Absorbance\ at\ 0\ hour} \quad \text{(Equation 1)}$$

NIR laser-induced temperature increase in vitro

Into a 96-well plate, 100 µL of PBS, PEGSH-AuIONP with a concentration of 10 and 50 ppm were exposed with NIR laser (808 nm) to irradiate the samples for 5 min. The changes of temperature were recorded at 0.5, 1, 2, 3, 4, and 5 minutes by an infrared camera (FLIR C2).

Flow Binding Assay

A site-specific atherothrombosis microfluidic device developed by Ta group was employed to evaluate the targeted binding of scFv labelled AuIONPs. Platelets were labelled with DiOC6 (0.5 µg/mL) before perfusion for fluorescence observation. The blood was infused through the main channel using the withdrawal option of the syringe pump at a rate of 4.998 µL/min, which corresponds to the physiological arterial shear rate of 1,000 s^{-1}. After 15 min of perfusion, a desirable size of thrombus was formed on the exposed GEL-COL composite hydrogel. The main channel was then washed by perfusing 0.5% BSA in PBS for 5 min at a shear rate of 5000 s^{-1} until removed all blood cells. AuIONP$^{(+)}$ with a concentration of 250 µg/mL in BSA 0.5% PBS 7.4 solution was perfused through the main channel by a syringe pump at a shear rate of 1,000 s^{-1} for 15 min, and binding of the NPs on thrombus was observed

under a microscope. AuIONP$^{(-)}$ with similar concentration was used as negative control and treated with similar procedures to the AuIONP$^{(+)}$ to check the nontargeted binding affinity of the NPs with thrombus. Brightfield and fluorescence images were taken at 200× magnification using an inverted microscope (CKX53, Olympus) mounted with a digital camera (DP74, Olympus). CellSens software Version 3.1 was used to compare the thrombus size and occlusion time in different stenosis at 5 min intervals. The same optic system recorded all images, otherwise mentioned. Data (n=3) was analysed by image processing software ImageJ (Java 1.8.0_172).

Cell Viability Assay

We evaluated the influence of AuIONP on cellular viabilty with the resazurin-based PrestoBlue reagent (Invitrogen). Macrophage RAW 264.7 cells with a density of 10,000 cells /well, were seeded into 96-well plates in 100 µL of cell culture medium, and incubated for 24 h to allow cell adherence. Cells were then incubated in the presence or absence of each of the AuIONP treatments for 24 h period, with untreated cells and cell culture medium alone used as positive and negative controls respectively. Cell viability was measured according to the manufacturer's instructions. Briefly, the PrestoBlue solution was added into each well and incubated for 30 mins at 37 °C. Fluorescence was measured on a plate reader (Clariostar, BMG Labtech) at a wavelength of 560/590 nm. To further confirm live cells, the cells were treated with calcein AM (Invitrogen) for 1 hour and fluorescence images were taken with Olympus microscope (excitation/emission).

Cell Viability Assay After Laser Exposure

To observe the effect of laser exposure towards healthy cells, cell viability was analysed using endothelial cells (SVEC4-10). Into a 96 well plate, endothelial cells (SVEC4-10) were seeded with a density of 8×10^3 per well, in 100 µL of cell culture medium, and incubated for 24 h. After 24 h, media was replaced by AuIONP 80 µg/ml or PBS as control solution and irradiated with laser at 1.5 W/cm^2 for 3 minutes x 3 cycles. Cell viability was measured using PrestoBlue and calcein AM solution, similar to the previously described procedure.

Haemolysis Percentage

Blood was centrifuged at 1000 rpm for 15 minutes to separate plasma with red blood cells. The red blood cells were obtained by separating the plasma and followed by washing of the red blood cells twice with PBS. A stock of red blood cells was created by diluting 1 mL of

washed red blood cells into a final volume of 50 ml with PBS. As much as 20 µL of liquid metal and AuIONP sample was placed in a well of a 96 well plate and 180 µL of the red blood cells stock solution was added. 1% Triton-X 100 and PBS were used as positive and negative control respectively. The plate was then placed in a shaking incubator at 37°C for 1 and 4 hours. After incubation, the plate was then centrifuged at 1000 rpm for 5 minutes and the supernatant was aspirated to transfer to a different well plate for reading. The samples were then observed for absorbance using a plate reader at 545 nm. Percent haemolysis was calculated using the equation below (Equation 2).

$$Haemolysis\ (\%) = \frac{Absorbance\ sample - Absorbance\ negative\ control}{Absorbance\ positive\ control - Absorbance\ negative\ control}\ x\ 100 \quad \text{(Equation 2)}$$

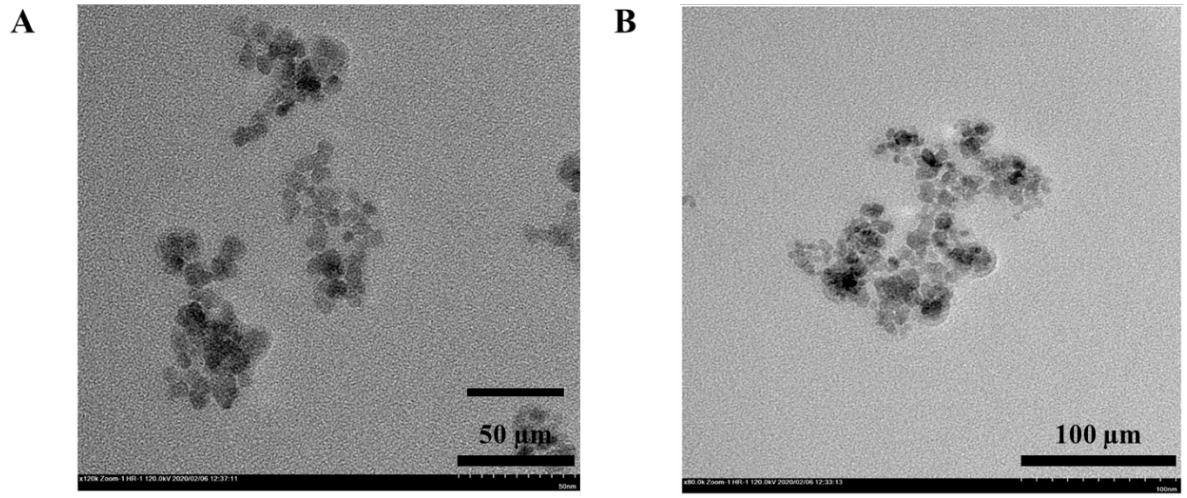

Figure S1. Transmission electron microscope (TEM) morphological images of the iron oxide cluster nanoparticle IONP with (A) 120000x and (B) 80000x magnification

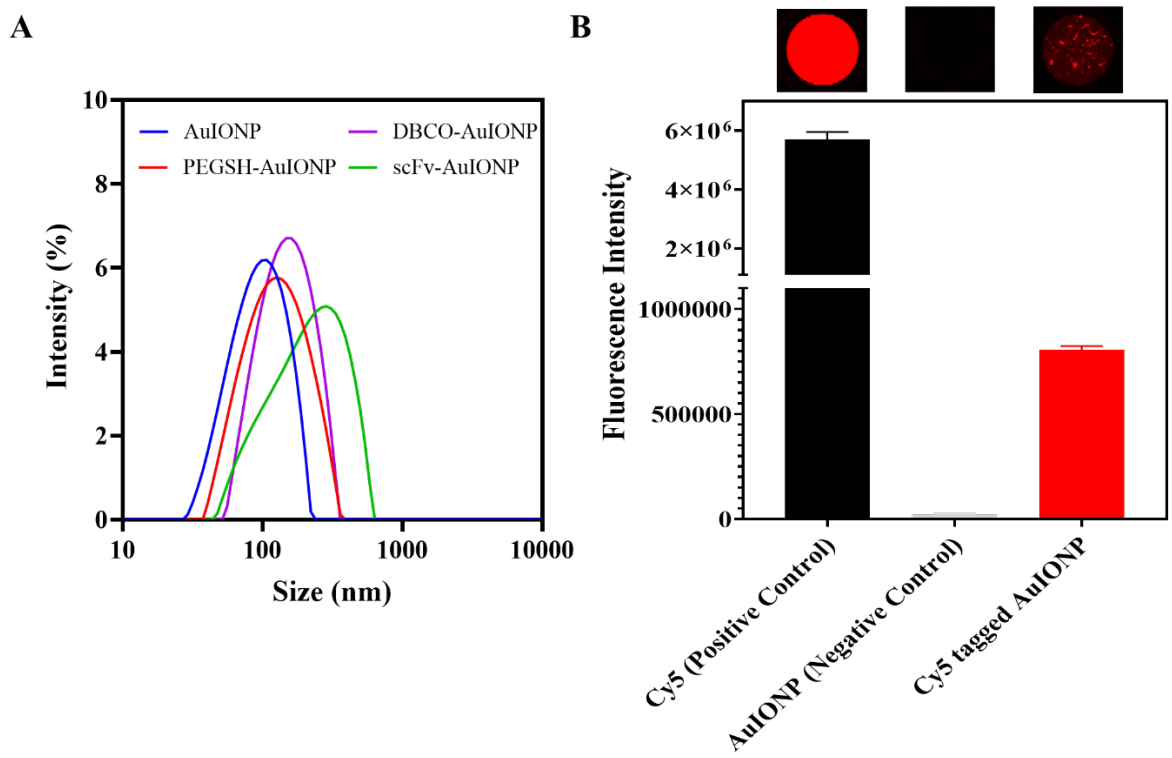

Figure S2. (A) Size distribution comparison of AuIONP, PEGSH-AuIONP, DBCO-AuIONP and scFv-AuIONP. (B) Fluorescence intensity of the obtained scFv-AuIONP with different addition method. Insert images are fluorescence intensity taken with Azure Sapphire system

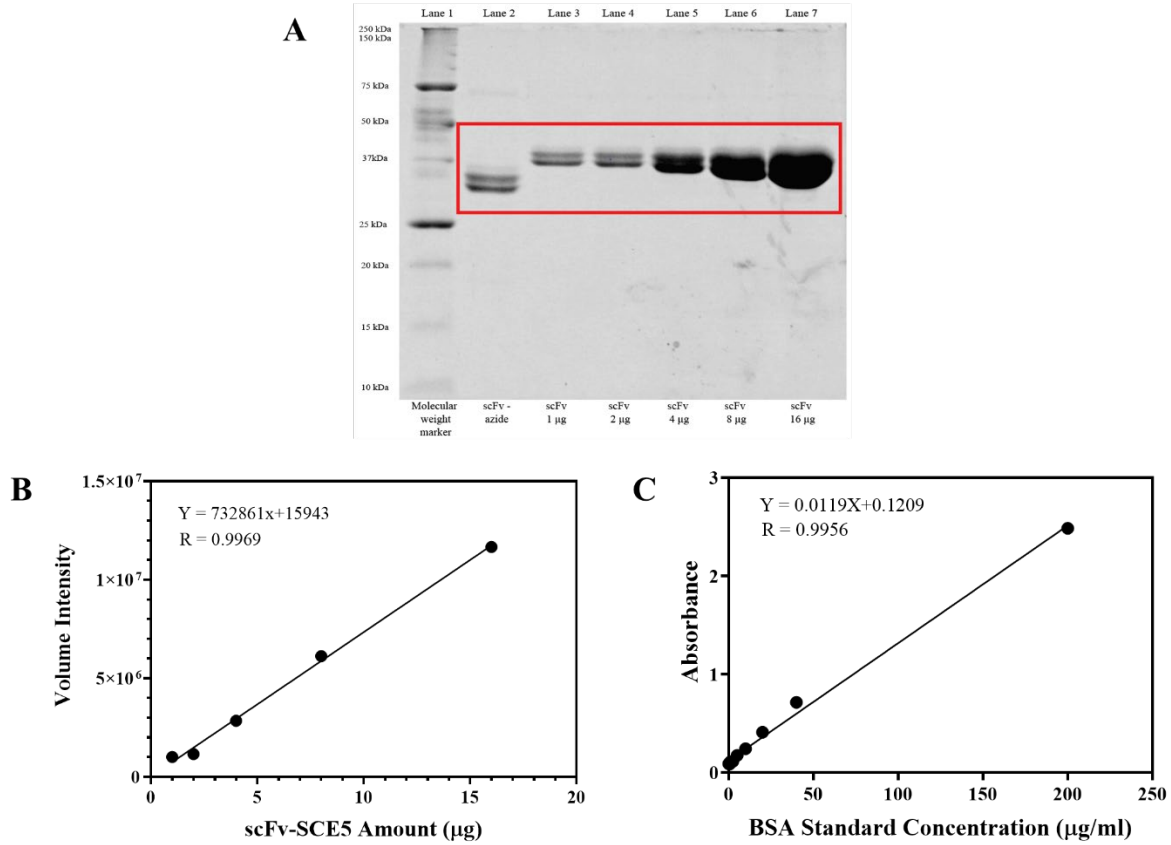

Figure S3. (A) SDS-PAGE gel result of scFv-SCE5 conjugation to GGG-N_3 peptide (lane 2), along with increasing concentration of scFv-SCE5 (lane 3-7); with (B) graph plotting of volume signal intensity after Coomasie blue staining and (C) BSA standard curve for BCA assay quantification

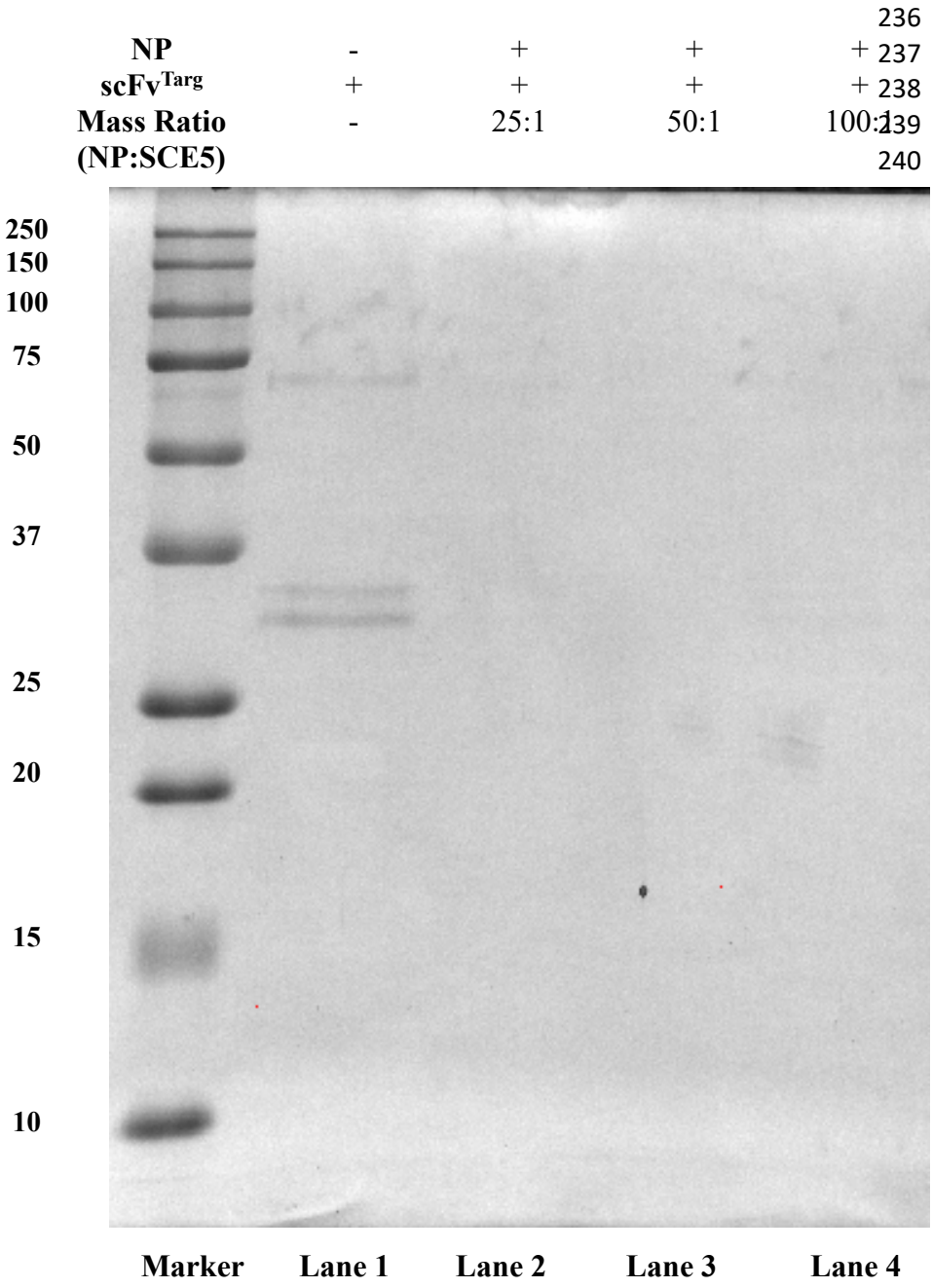

Figure S4. SDS-PAGE of scFv after conjugation with DBCO-AuIONP with different ratio of antibody. The disappearance of the scFv band from lane 2 to 4, indicated the scFv was successfully attached to the DBCO-AuIONP.

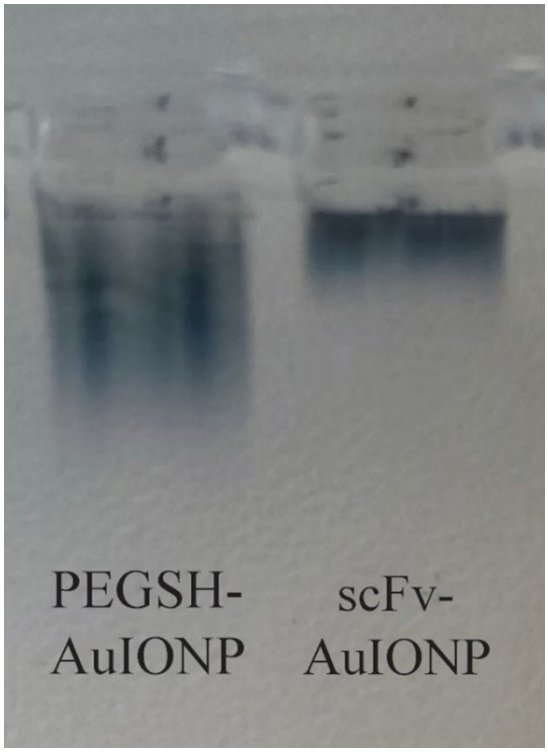

Figure S5. Agarose gel electrophoresis result of the particle. PEGSH-AuIONP is more negatively charged and has a smaller size compared to scFv-AuIONP, causing more significant migration in the gel layer.

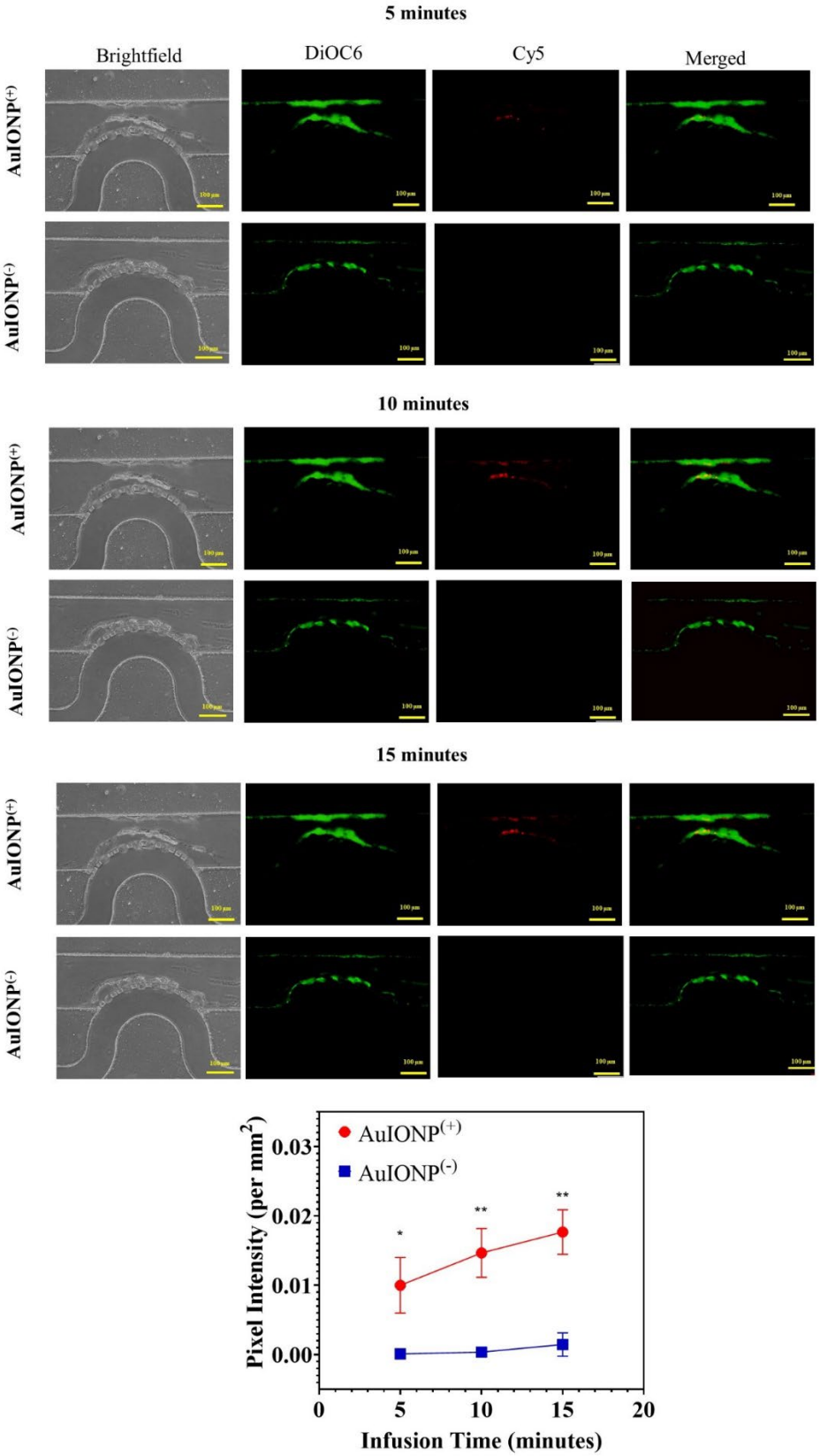

Figure S6. Top pictures showcased the increase of platelet targeted Cy5-tagged AuIONP ($AuIONP^{(+)}$) over time as compared to the nontargeted particles ($AuIONP^{(-)}$) (scale bar = 100 μm). The graph represents the pixel intensity of particles binding on thrombus observed over time

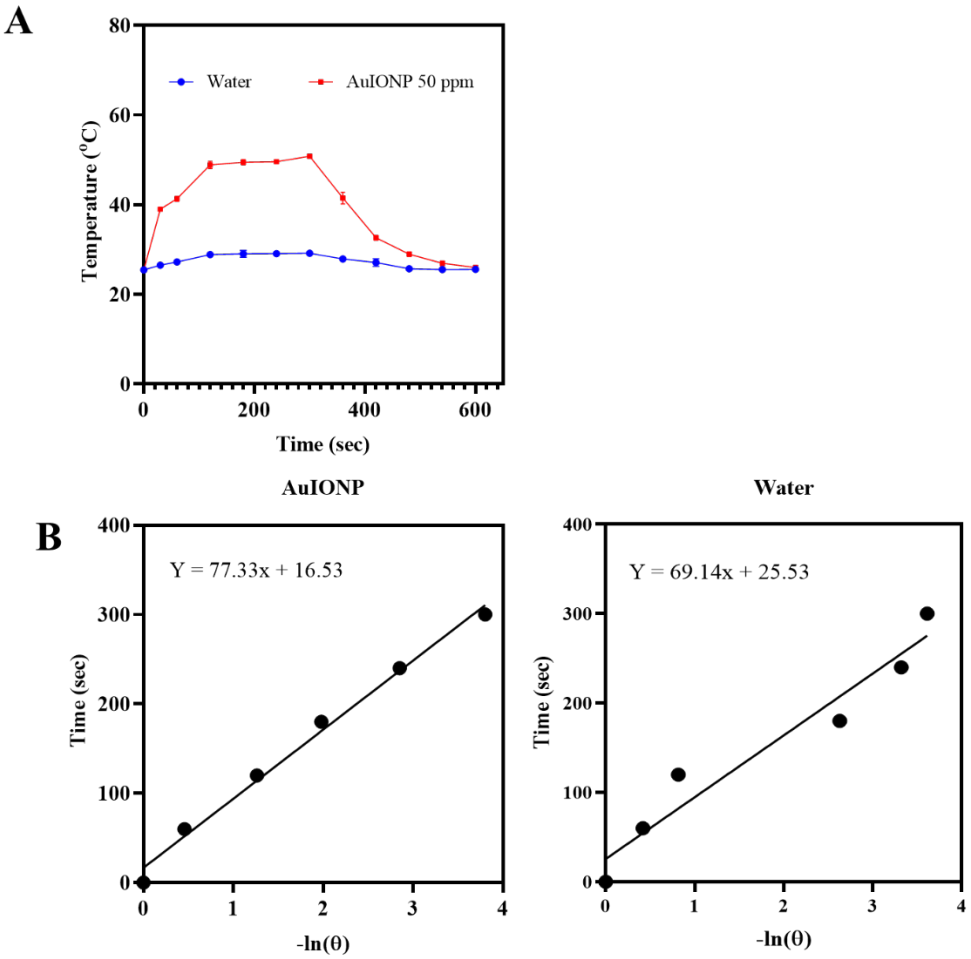

Figure S7. Calculating photothermal conversion efficiency. (A) Temperature change of AuIONP with a concentration of 50 ppm and water with NIR irradiation for 300 seconds (808 nm, 1.5 W/cm^2). After 300 seconds, the laser was shut off and temperature was observed for additional 300 seconds. (B) Plot of -ln(Θ) vs time of the cooling period to calculate the photothermal conversion efficiency Based on Qian et al. report, total energy balance for the photothermal system can be explained with Equation 3 below:

$$\sum_i m_i C_{p,i} \frac{dT}{dt} = Q_{AuIONP+} Q_{Dis} - Q_{Surr} \quad \text{(Equation 3)}$$

m = mass (g)
C = heat capacity (J/g °C)
T = temperature of solution (°C)
t = time (second)
Q_{AuIONP} = energy by AuIONP
Q_{Dis} = energy from container and solvent
Q_{surr} = energy dissipated away from the system by surrounding or air

Energy generated by AuIONP can be quantified using the following (Equation 4):

$$Q_{AuIONP} = I\,(1 - 10^{-A_{808}})\,\eta \quad \text{(Equation 4)}$$

I = laser intensity (W)

A_{808} = absorbance of AuIONP at 808 nm
η = photothermal conversion efficiency

Furthermore, Equation 3 can be simplified after the laser intensity has been defined, as the amount of energy by AuIONP and the energy from solvent and container ($Q_{AuIONP} + Q_{Dis}$) will be finite. Based on that, AuIONP photothermal conversion efficiency (η) can be calculated using Equation 5 below :

$$\eta = \frac{hs\,(T_{max} - T_{surr}) - Q_{Dis}}{I(1 - 10^{-A_{808}})} \quad \text{(Equation 5)}$$

h = heat transfer coefficient
s = surface area of the container
Tmax = maximum temperature obtained with laser irradiation
Tsurr = initial temperature before the laser irradiation

hs can be determined by obtaining a dimensionless parameter Θ and a sample system time constant which can be calculated by the following Equation 6 and 7 respectively

$$\Theta = \frac{T - T_{surr}}{T_{Max} - T_{Surr}} \quad \text{(Equation 6)}$$

$$t = -\tau_s \, ln\,(\Theta) \quad \text{(Equation 7)}$$

where $\boldsymbol{\tau}_s$ can be determined by obtaining the slope value of -ln(Θ) vs time (Figure S7B) from the cooling period of the observation. From our calcThis is then followed by calculating hs with Equation 8:

$$hs = \frac{m\,C}{\tau_s} \quad \text{(Equation 8)}$$

Based on this, we obtained $\boldsymbol{\tau}_s$ value for AuIONP and water as 77.33 and 69.14 respectively. Additionally, the m for AuIONP was 50 µg and C was 4.2 J/g·℃. With knowledge of the absorbance value at 808 nm (A_{808}) value from 50 ppm of AuIONP was 0.4849 and laser intensity exposed was 1.5 W/cm^2, we then insert these values into Equation 5 to obtain η which we retrieved to be 37.47%.

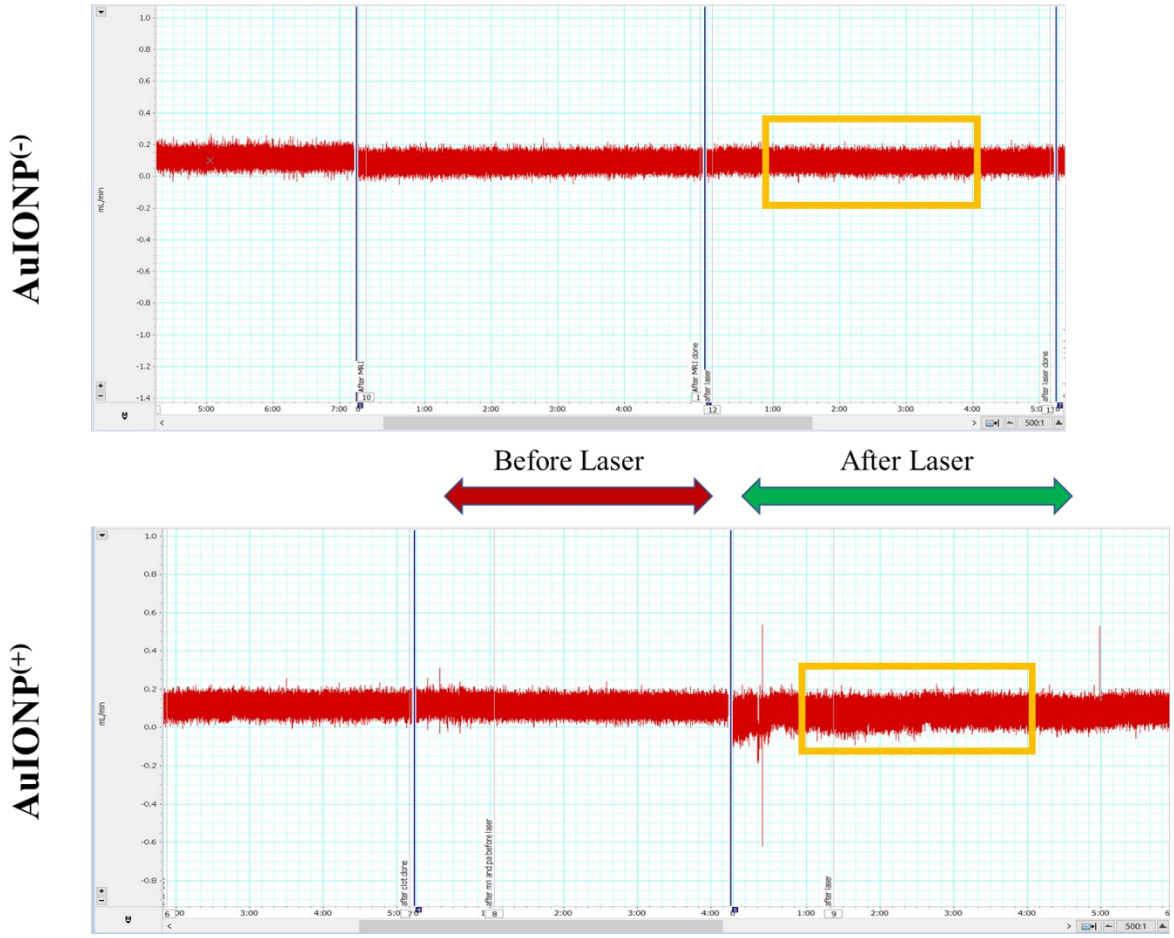

Figure S8. Difference of blood flow (ml/min) observed with flow probe. AuIONP$^{(+)}$ treated groups produced higher change in blood flow shown by the wider range of maximum value to minimum value between the observed time range (orange box) compared to the AuIONP$^{(-)}$ group.

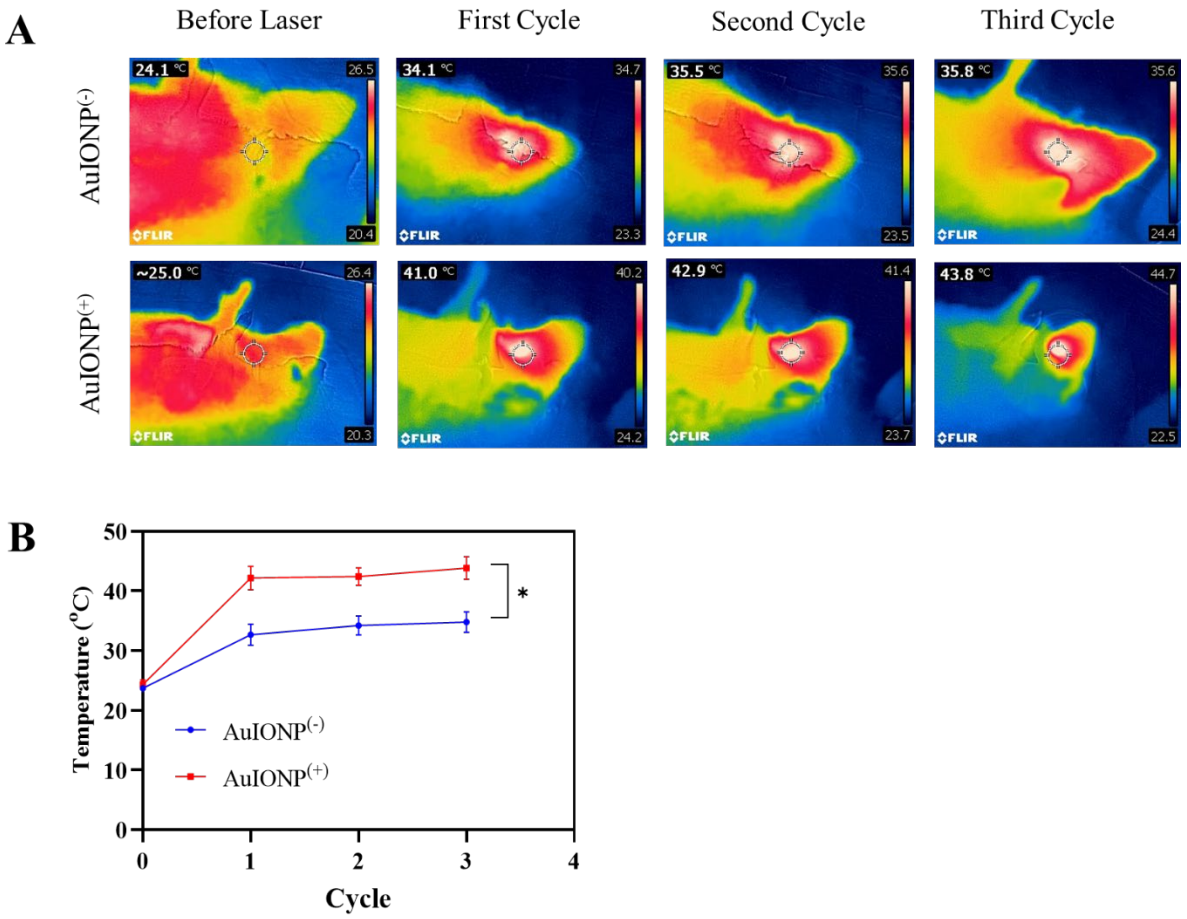

Figure S9. (A) Infrared thermal images of AuIONP$^{(+)}$ and AuIONP$^{(-)}$ after each cycles and (B) graph illustrating the temperature observed after each cycle of laser exposure in vivo

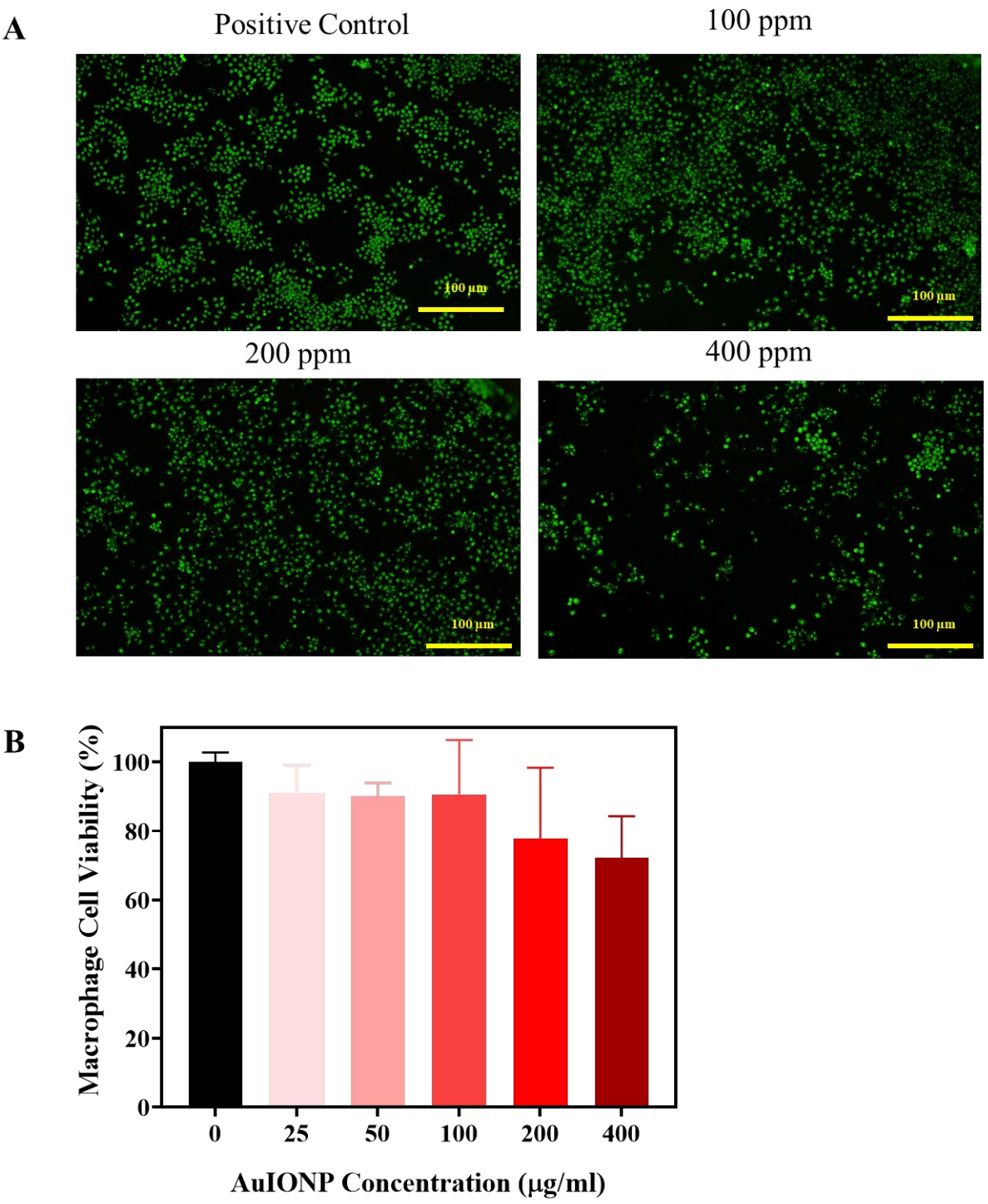

Figure S10. (A) Images of macrophage stained with calcein AM after incubated with AuIONP for 24 hours and (B) the respective result of cell viabilty after the incubation

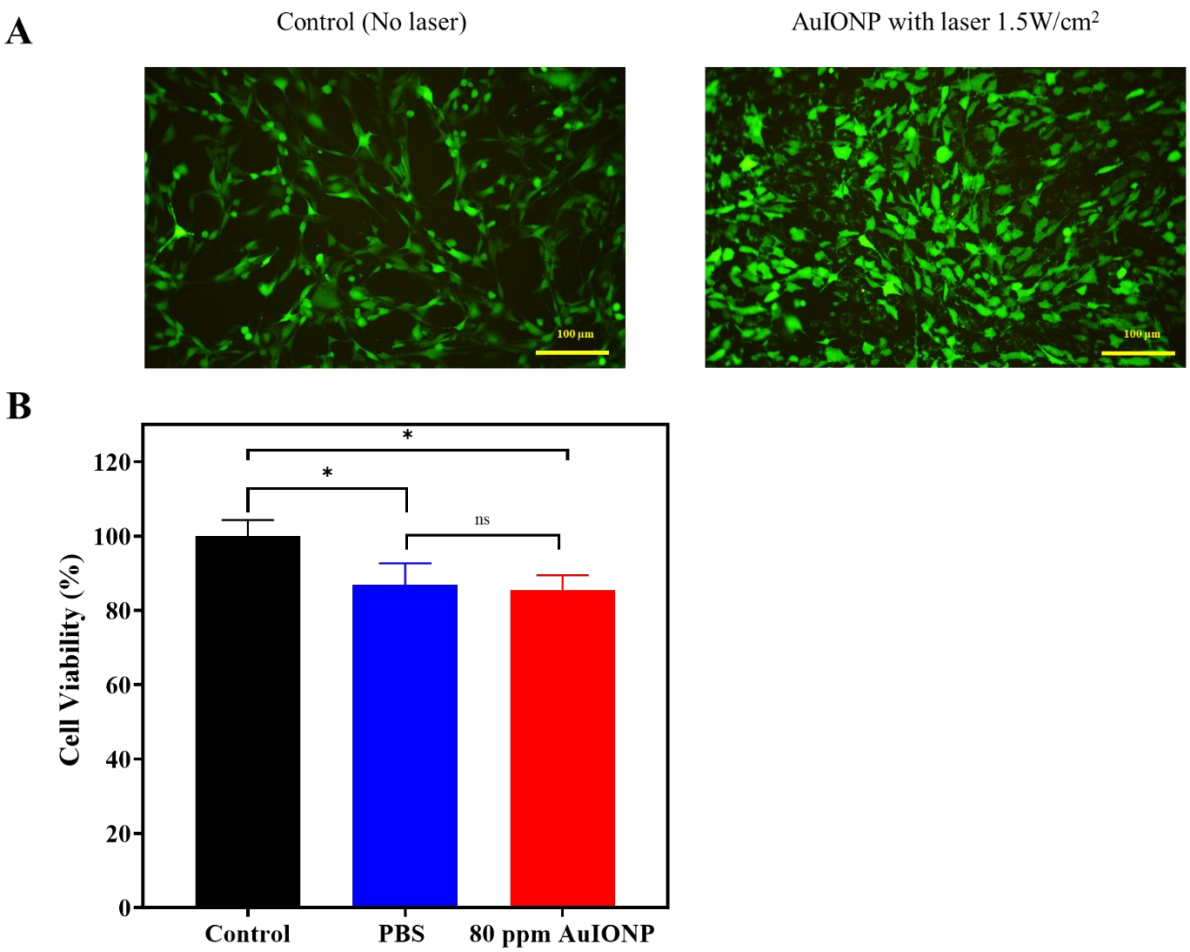

Figure S11. **Cell Viability After Laser Exposure** (A) Microscope images of endothelial cells, after exposed with laser 808 nm at 1.5 W/cm^2 and 3 minutes x 3 cycles of exposure time. (B) Cell viability calculation indicated there was no significant difference between the PBS group and the AuIONP samples.

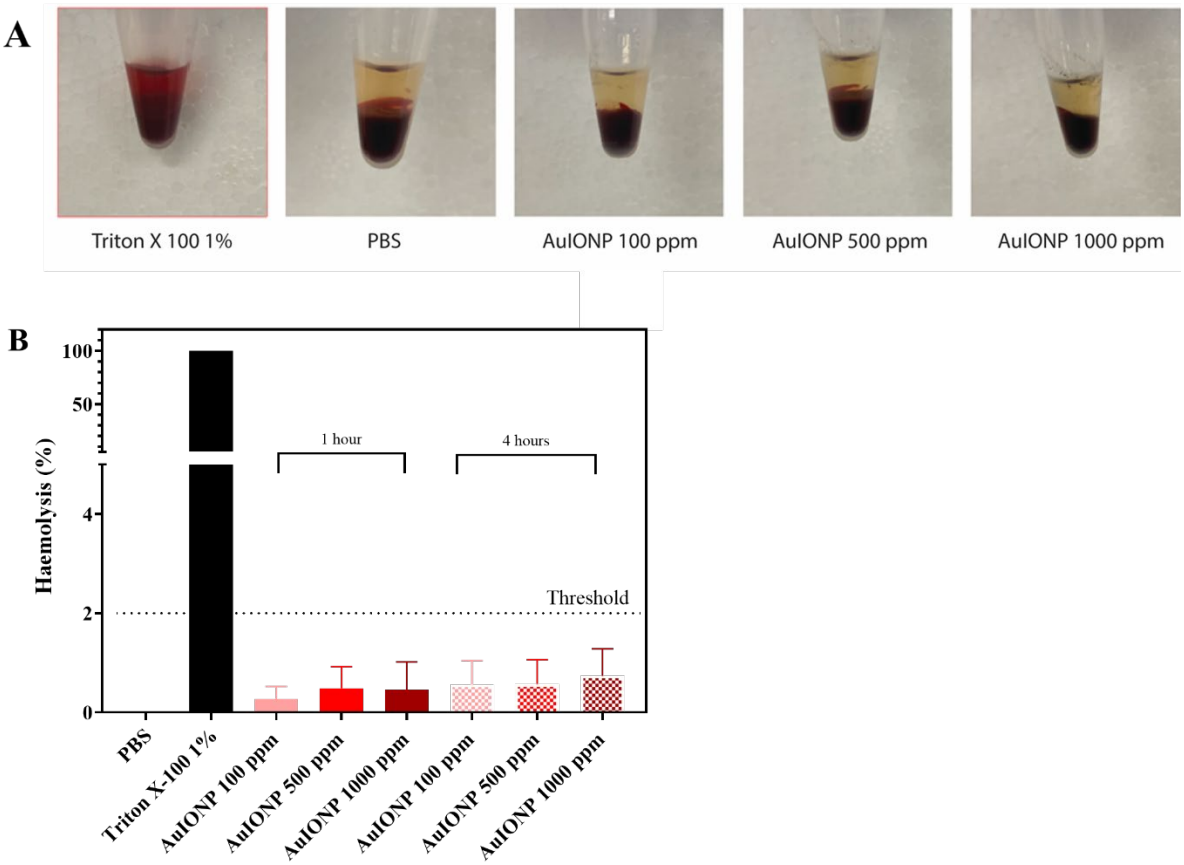

Figure S12. Haemolysis observation and percentage. (A) Haaemolysis observation on AuIONP. Appearance of whole blood samples after 4 hours of incubation, with plasma appearing clear yellowish, similar to the PBS group. (B) AuIONP groups with various concentrations did not have any significant difference in haemolysis percentage compared to PBS treated group, and were all below threshold of 2%, indicating AuIONP did not induce haemolysis.

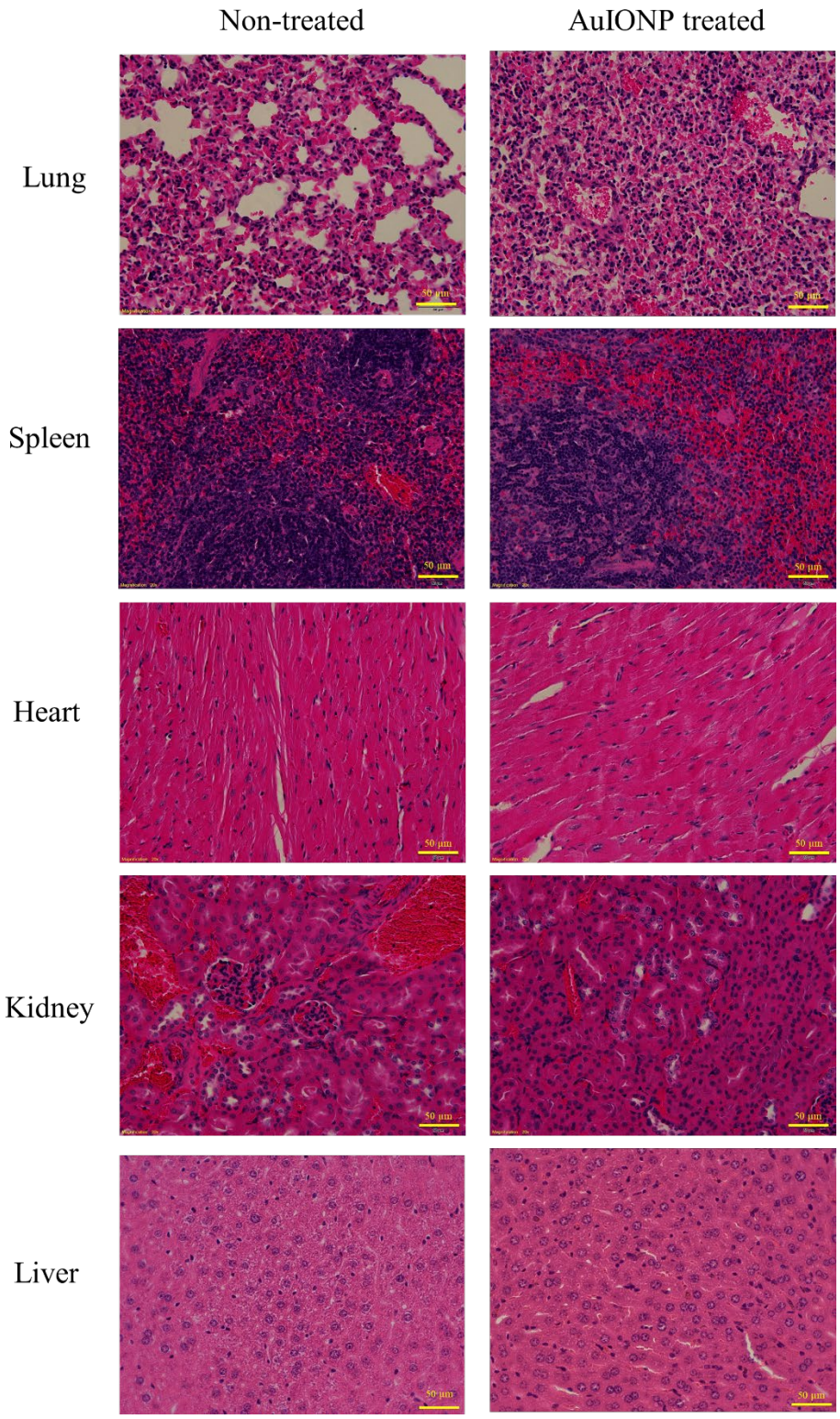

Figure S13. Microscopic observation of the organs from non-treated control (no injection of NPs) and 5 hours post injection of the nanoparticle. Tissues were stained with hematoxylin eosin and no visible difference was noticed between the groups (scale bar = 50 µm).

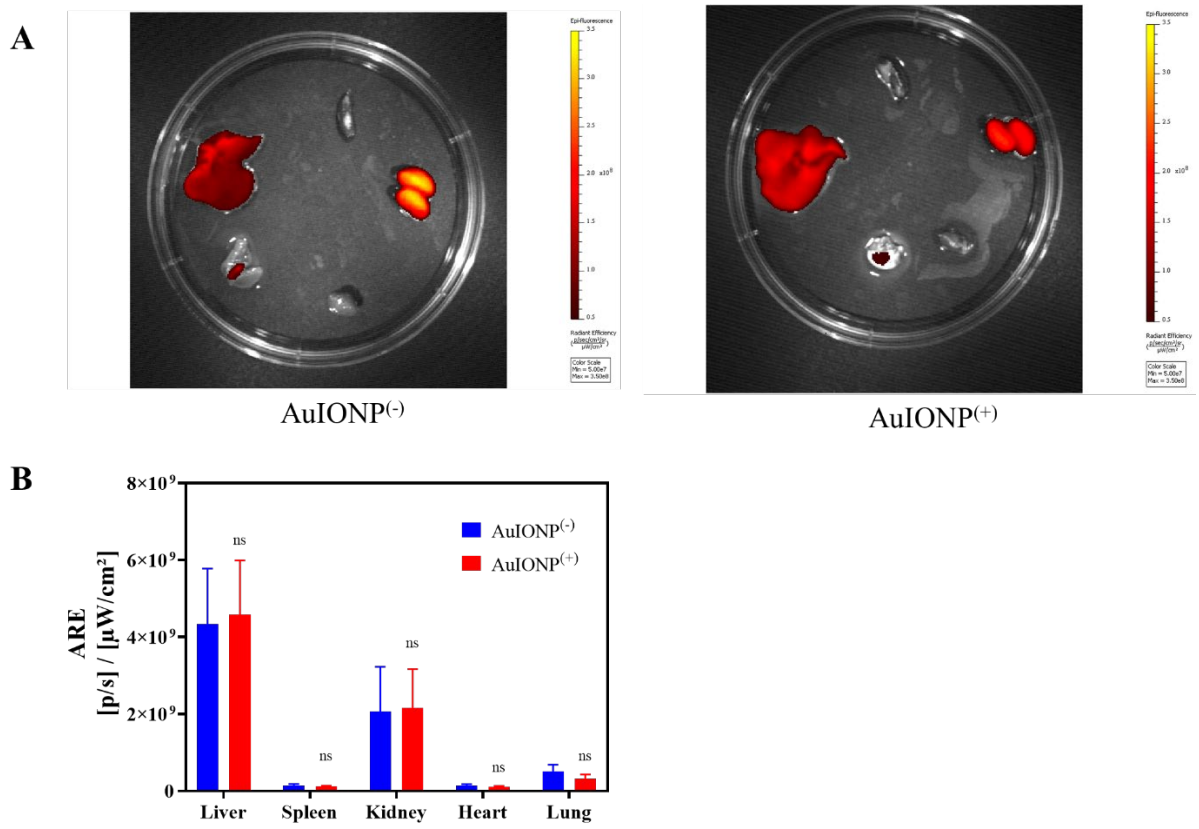

Figure S14. Ex vivo fluorescence intensity and images of organs. (A) Overlayed image of the black and white photograph and the fluorescence image of ex-vivo organ observation. From top clockwise: spleen, kidney, heart, lung, and liver. (B) Analysis of the average radiant efficiency (ARE) indicated there is no significant difference of fluorescent present in the organs listed between AuIONP$^{(-)}$ and AuIONP$^{(+)}$ groups.

Calculating the number of scFv molecules conjugated to an AuIONP:

In order to calculate number of molecules of antibody attached to a given particle we first need to calculate number of particles in a known mass. We can calculate this using Equation 1 and 2 below:

$$Mass\ of\ one\ particle = density \times volume\ of\ particle$$

(Equation 1)

$$Number\ of\ particles\ in\ a\ known\ mass = \frac{mass\ of\ sample}{mass\ of\ one\ particle} \qquad \text{(Equation 2)}$$

For the reaction we used PEGSH-AuIONP 1 mg with a size 120 nm. Due to the arbitrary shape of the nanorose structure, we cannot use the nanorose structure to calculate volume, so for the purpose of calculation we assume the particle is spherical. Additionally, based on these information we calculate the number of particles using the equations above:

Density of Au = 19.32 x 10^3 mg/cm^3

Volume of AuIONP (sphere) = $\frac{4}{3} \times \pi \times r^3 = \frac{4}{3} \times 3.14 \times 60^3 = 9.04 \times 10^{-16}\ cm^3$

Mass of one AuIONP particle = (19.32 x 10^3 mg/cm^3) x (9.04 x10^{-16} cm^3)

405 $= (1.75 \times 10^{-11})$ mg

406 So, the number of particles in 1 mg = $\frac{1\ mg}{1.75 \times 10^{-11}\ mg}$ = 5.72 x 10^{10} particles

407 After obtaining the number of particles, utilised for the conjugation, using mole equation
408 described with Equation 3 and 4 below:

409 $$Mole\ of\ antibody = \frac{mass\ of\ antibody}{molecular\ weight\ of\ antibody}$$ (Equation 3)

410 $$Number\ of\ molecules = mole \times Avogadro\ number$$ (Equation 4)

411 Based on the information of antibody conjugation, we then calculate the mole of antibody based
412 on the yield we obtained from BCA (62% of 20 µg of $scFv_{SCE5}$, MW: 33 kDa), with details as
413 follow:

414 Mole of $scFv_{SCE5}$== $\frac{12.4\ \mu g}{33000\ g/mole} = 3.76 \times 10^{-10}\ mole$

415 Number of molecules of antibody = $3.76 \times 10^{-10}\ mole \times 6.02 \times 10^{23} = 2.26 \times 10^{14}$
416 molecules

417 After obtaining these information, we can calculate the rate of antibody conjugated with
418 Equation 5:

419 $$Rate\ of\ conjugation = \frac{number\ of\ antibody\ molecules}{number\ of\ particles}$$ (Equation 5)

420 So, the rate of antibody conjugation per molecule of PEGSH-AuIONP = $\frac{2.26 \times 10^{14}}{5.72 \times 10^{10}}$

421 = 3.95 x 10^3 antibodies/particle

422 The number of antibodies was conjugated to PEGSH-AuIONP with overnight (16 hours)
423 incubation period. This amount of antibody is considered sufficient and highly conjugated [1].

424

425

426 [1] B. Saha, T.H. Evers, M.W. Prins, How antibody surface coverage on nanoparticles determines the
427 activity and kinetics of antigen capturing for biosensing, Anal Chem 86(16) (2014) 8158-66.

428